 doi:10.20944/preprints202108.0457.v1

Review

A Review on Rhenium Disulfide: Synthesis Approaches, Optical Properties, and Applications in Pulsed Lasers

Mahmoud Muhanad Fadhel [1], Norazida Ali [1], Haroon Rashid [1], Nurfarhana Mohamad Sapiee [1], Abdulwahhab Essa Hamzah [1], Mohd Saiful Dzulkefly Zan [1], Norazreen Abd Aziz [1] and Norhana Arsad [1,*]

[1] Department of Electrical, Electronic and Systems Engineering, Faculty of Engineering and Built Environment, Universiti Kebangsaan Malaysia, UKM Bangi 43600, Selangor, Malaysia; P97209@siswa.ukm.edu.my (M.M.F); P96194@siswa.ukm.edu.my (N.A); haroon@ukm.edu.my (H.R); P103517@siswa.ukm.edu.my (N.M.S); P97926@siswa.ukm.edu.my (A.E.H); saifuldzul@ukm.edu.my (M.S.D.Z); norazreen@ukm.edu.my (N.A.A)

* Correspondence: noa@ukm.edu.my

Abstract: Rhenium Disulfide (ReS_2) has evolved as a novel 2D transition-metal dichalcogenide (TMD) material which has promising applications in optoelectronics and photonics because of its distinctive anisotropic attributes. In this review, we emphasize on formulating saturable absorbers (SAs) based on ReS_2 to produce Q-switched and mode-locked pulsed lasers of diverse operation wavelengths like 1 μm, 1.5 μm, 2 μm, and 3 μm. We outline ReS_2 synthesis techniques and integration platforms concerning solid-state and fiber-type lasers. We discuss the laser performance based on SAs attributes. Lastly, we draw conclusions and outlook by recommending additional improvements for SA devices so as to advance the domain of ultrafast photonic technology.

Keywords: saturable absorbers; Rhenium disulfide; pulsed lasers; mode-locking; Q-switching; 2D TMD

1. Introduction

Ultrafast laser technology pertains to the creation, amplification, and operation of ultrashort pulses with periods ranging from nanosecond to picosecond and femtosecond. Numerous distinct characteristics of pulsed lasers like greater peak intensity, broad spectrum, and fast temporal resolution [1] have driven a wide-range of uses like laser welding and drilling [2], ultrafast spectroscopy [3,4], and frequency comb metrology [5,6]. Furthermore, pulsed lasers based on intensity modulation have proven their significant efficiency within a wide variety of distributed optical fiber sensors (DOFS) [7-11]. These kinds of lasers could be produced either by Q-switching or mode-locking methods, which are categorized into passive or active modulation methodologies. Typically, the Q-switching method can provide immense short-duration pulses in the microsecond to nanosecond range by regulating cavity loss frequently using a kilohertz-range frequency. On the other hand, the mode-locking method [12] comprising a concurrent in-phase lock of all the longitudinal modes in the cavity is frequently employed for producing extremely-short pulses ranging from a few femtoseconds to several picoseconds. Furthermore, the mode-locked pulse repetition rate is quite higher compared to the Q-switching repetition rate [13].

The active modulation technique relies on an optical modulator with an externally-applied modulating signal; the modulator is usually based on the electro-optic or acousto-optic effect [1,14]. Even though this methodology is quite robust, it fails to create very short pulses because of the inadequate bandwidth of active modulators. Conversely, passive modulation designs are in a position to offer quite shorter pulses, as the SA with a brief recovery time can regulate the cavity loss much quicker compared to an electronic optical modulator [15].

Preprints (www.preprints.org) | NOT PEER-REVIEWED | Posted: 23 August 2021 doi:10.20944/preprints202108.0457.v1

The saturable absorbers in passive Q-switching and mode-locking approaches could be generally split into two classes: real SAs, materials which demonstrate an intrinsic nonlinear drop in absorption with growing light intensity; and artificial SAs, devices which manipulate nonlinear effects, like nonlinear polarization rotation (NPR) and nonlinear amplifying loop mirror (NALM), to simulate the action of a real SA by provoking an intensity-dependent transmission [16]. Nevertheless, NPR and NALM face several issues, like high saturable threshold power and polarization sensitivity [17].

The advancements in microfabrication and material science have driven a growing number of materials which could be utilized as real SAs. Figure 1 depicts the progression of real SA technologies and their applications as photonic devices. In 1964, "reversibly bleachable" dye [18] and colored glass filters [19] were used for the first-ever presentation of SA-based pulse generation by Q-switching a ruby laser, just four years after Maiman demonstrated laser operation [20]. Reversibly bleachable dyes were extensively deployed to mode-lock lasers, driving the first exhibition of continuous-wave (CW) mode locking [21]. Later in 1983, ion-doped fiber has emerged as gain medium, and unstable mode-locking of a Nd:Fiber laser was reported using a dye SA [22]. It was quite challenging to create steady mode-locked pulses among fiber lasers, till the exhibition of semiconductor saturable absorber mirror (SESAM) in 1992 [23], a discovery which facilitated the first display of a passively mode-locked fiber laser (Nd:YLF) minus Q-switching instabilities. However, producing SESAMs typically comprises sophisticated and highly specialized instruments. Post-growth ion insertion or the uses of low temperature growth are employed for minimizing device response time. Additionally, a typical SESAM-based instrument operates in a narrow wavelength band (<100 nm) [1].

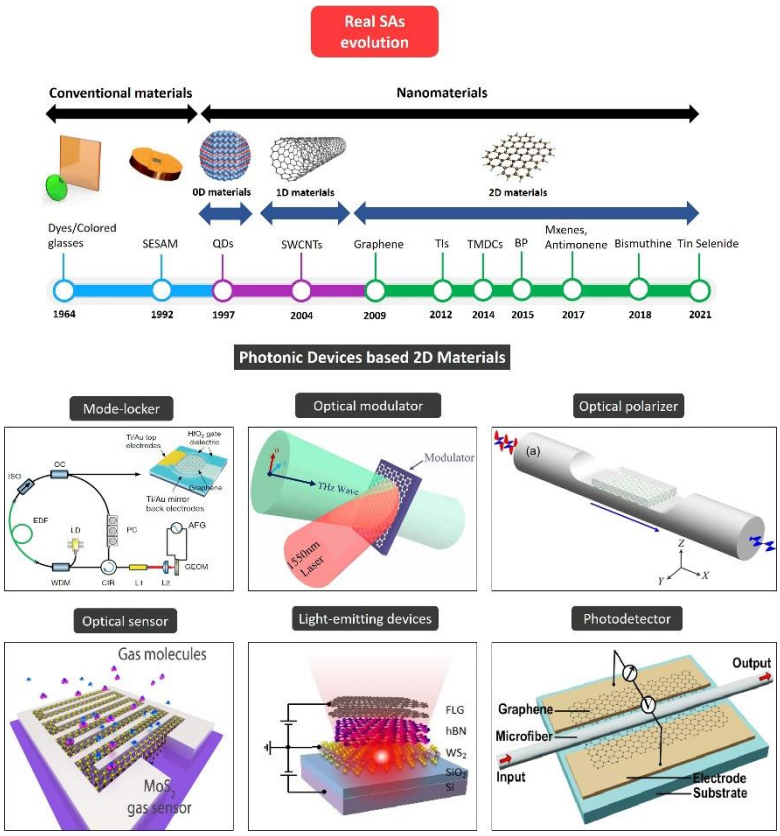

Figure 1. The evolution of real saturable absorber technologies and their applications as photonic devices. Ref. [24]; reproduced with permission; copyright 2018, John Wiley and Sons. Ref. [25]; reproduced under the terms of a Creative Commons Attribution 4.0 International License; copyright 2014, Springer Nature. Ref. [26]; reproduced under the terms of a Creative Commons Attribution 4.0 International License; copyright 2016, Springer Nature. Ref. [27]; reproduced under the terms of a Creative Commons Attribution 4.0 International License; copyright 2015, Springer

Preprints (www.preprints.org) | NOT PEER-REVIEWED | Posted: 23 August 2021 doi:10.20944/preprints202108.0457.v1

Nature. Ref. [28]; adapted with permission; copyright 2017, American Chemical Society. Ref. [29]; reproduced under the terms of a Creative Commons Attribution 4.0 International License; copyright 2015, The Optical Society.

Unfortunately, such traditional SA materials have certain disadvantages, and therefore are not able to fulfill the main SA requirements, like fast response time, strong nonlinearity, low loss, broad bandwidth, greater power handling, and low costs [30]. SA material with nanometer-scale dimensionality may offer pronounced optoelectronic characteristics and powerful quantum confinement [31]. In 1997, zero-dimensional quantum dots (QDs) were used for pulse generation [32]. This presentation led to widespread interest in nanomaterial SAs. One-dimensional single-walled carbon nanotubes (SWCNTs) [33] and two-dimensional graphene [34] were regarded as potent materials for creating ultrafast pulses in the sub-picosecond range [30]. Usually, nanotubes with distinct diameters and chirality are tough to synthesize [35].

Apart from graphene, which was originally found in 2004 [36] with zero-bandgap structure, there are a broader category of novel 2D materials like topological insulators (TIs) [37,38], transition metal dichalcogenides (TMDs) [39,40], black phosphorus (BP) [41,42], MXenes [43], antimonene [44,45], bismuthine [46-48], and tin selenide [49]. Nowadays, 2D materials are a preference for research and use in nearly each domain of science and engineering, especially TMDs which demonstrate adaptable chemistry.

TMDs having MX_2 chemical formula typically comprise a plane having hexagonally-placed transition metal atoms M (groups 4-10) in Figure 2 placed between two chalcogen atom-based hexagonal planes X (e.g., S, Se, Te). The M-X bonds within layers are mostly covalent, while weak Van der Waals forces hold the sandwiched layers [50]. TMDs have been acknowledged since the 60s, and a set of 40 TMDs and their elementary attributes was reviewed in 1969 [51]. Members of Group 6 like WSe_2 and MoS_2 are the most distinctive ones; yet, rhenium disulfide (ReS_2) in group 7 has been drawing the highest attention recently due to its uncommon electro-optical, structural, and chemical attributes [52]. Contrasting to group 6 TMDs which steadied in extremely symmetric 2H structures, ReS_2 possesses a distinctive distorted 1T structure that renders an in-plane anisotropy to its physical attributes [53]. Furthermore, because of the exceptionally weak interlayer coupling, bulk ReS_2 functions as vibrational and electronically decoupled monolayers, causing a noticeable layer-independent character in different attributes [54]. Such unique attributes of ReS_2 have encouraged several evolving applications such as catalysis, energy storage, optoelectronic devices, and sensing [55-57]. Considering the strong light absorbance in a wide wavelength band, ReS_2 material is potentially useful for optical modulation as required for pulsed lasers using SAs [58,59].

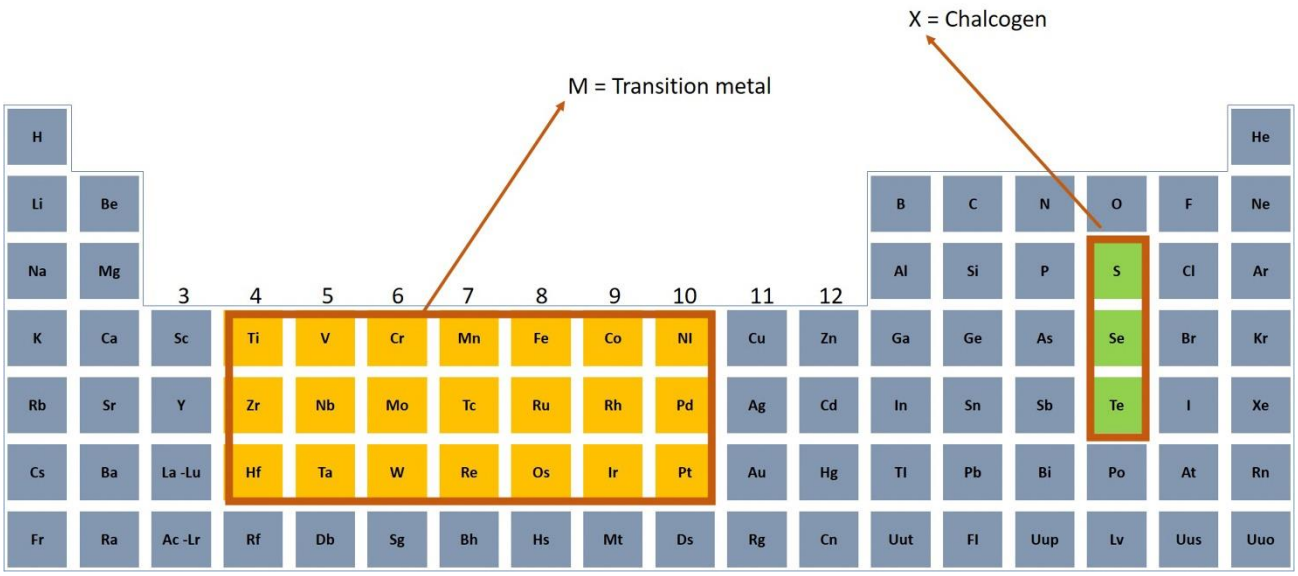

Preprints (www.preprints.org) | NOT PEER-REVIEWED | Posted: 23 August 2021 doi:10.20944/preprints202108.0457.v1

Figure 2. Periodic table showing TMDs materials with its components of transition metals M and three chalcogen X elements.

This review comprises a summary of the present state-of-the-art photonic devices based on ReS_2. We discuss the material production, integration, and use of SA devices for ReS_2 pulsed lasers. On the basis of these developments, a conclusion and point of view for new prospective opportunities for ultrafast photonic technologies are emphasized.

2. Rhenium Disulfide (ReS_2)

2.1. Atoms Arrangement and Band Structure

Noddack, Tacke, and Berg [60] were the first to discover rhenium in 1925, the last steady element in the periodic table [53]. The atomic arrangement of a ReS_2 layer may be understood as a distorted 1T arrangement. The layer comprises a zigzag Re-Re chains along the b-axis of the lattice (Figure 3a) [54]. Metal-metal bonding causes doubling on the ReS_2 unit cell, which, therefore, comprises eight S and four Re atoms (Figure 3b). Figure 3c depicts a less zoomed ReS_2 annular dark field (ADF) picture showing tri- and mono-layer regions on the flakes [61]. The ADF image clearly shows single layer regions comprising four Re atoms forming diamond-shaped links (green line).

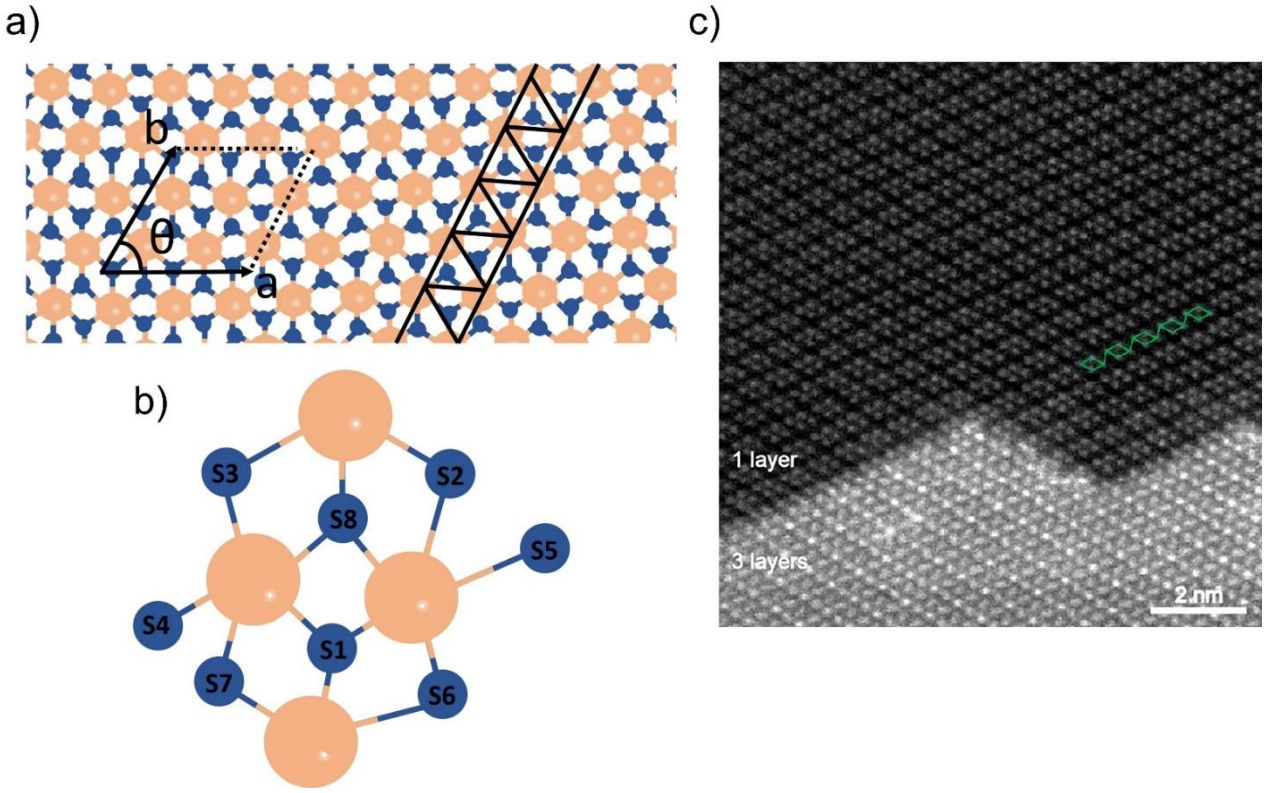

Figure 3. (a) Atomic structure of a monolayer ReS_2. Unit cell and Re chains are indicated. (b) Top view of the ReS_2 monolayer shown by unit cell atoms. (c) Low magnification ADF image of ReS_2. The upper part is single-layer with the diamond-shape (DS) phase structure, while the lower part is three-layer stacking. Reproduced with permission from Ref. [61]. Copyright 2015, American Chemical Society.

ReS_2 has a noteworthy aspect: the band structures for monolayer, trilayer and five-layer ReS2 are similar (Figure 4), indicating the nature of ReS_2 of maintaining a direct-bandgap [62]. On the other hand, several TMDs have direct and indirect bandgaps in monolayer and bulk forms, respectively [54]. Bandgap characteristics can cause thickness to affect TMD properties extensively. Furthermore, based on the strain as well as ribbon width, the bandgap and electronic properties of mono-layered TMDs will alter greatly

Preprints (www.preprints.org) | NOT PEER-REVIEWED | Posted: 23 August 2021 doi:10.20944/preprints202108.0457.v1

[63,64]. Ab initio calculations indicate that ReS_2 bandgap does not change significantly when the thickness is increased from monolayer (1.44 eV), trilayer (1.4 eV) to five-layer (1.35 eV) [62]. This distinct response can be attributed to the absence of interlayer registry and weak interlayer connection caused by Peierls distortion of the ReS_2 1T arrangement [54]. Additionally, the comparability of optical and electrical characteristics of single-layer and bulk ReS_2 indicates that the material could offer a base to evaluate 2D system mesoscopic physics without facing the challenge of producing thick monolayer flakes with substantial area [65].

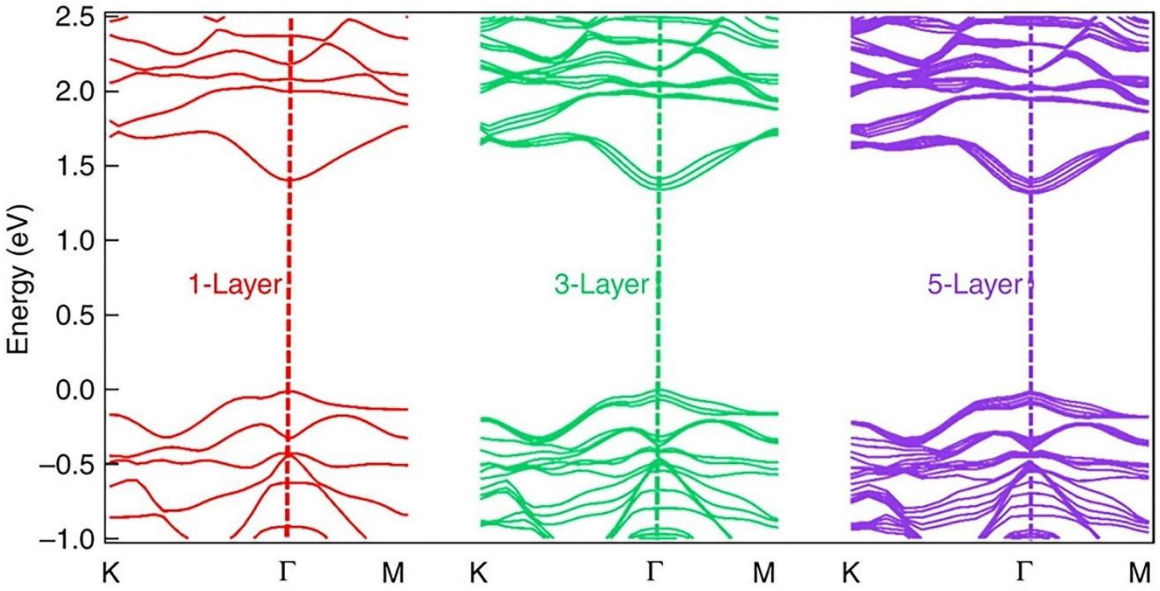

Figure 4. Ab initio calculated electronic band structure of monolayer, trilayer and five-layer ReS_2 indicating band gaps of 1.44, 1.4 and 1.35 eV, respectively. Reproduced under the terms of a Creative Commons Attribution 4.0 International License [62]. Copyright 2015, Springer Nature.

2.2. Optical Properties

ReS_2 in bulk form has anisotropic optical characteristics that are recorded [66]. The present emphasis is on the material comprising few layers and the monolayer structure [67]. Figure 5a depicts the photoluminescence (PL) spectrum of ReS_2 flakes with diverse quantity of layers [68]. Thinning of ReS_2 material form 7-layer to monolayer thickness is associated with a reduction in PL intensity. However, the red-shift associated with the peak position is insignificant, indicating little dependence on layer count. This observation is in agreement with theoretical bandgap calculations of ReS_2 [69].

The ReS_2's Raman response is shown in many research works [70-72]. Because of the low symmetry of ReS_2, a higher number of Raman modes could be seen as against the traditional TMDs. Additionally, the frequency shift for every Raman mode indicates minute changes concerning monolayer to bulk ReS_2, as shown in Figure 5b; the figure indicates 18 Raman modes corresponding to bulk, five-layer, and monolayer ReS_2 [62]. There are six Raman modes with labels; these comprise two Ag-like low-frequency modes (identified at 136.8 and 144.5 cm^{-1}) specific to out-plane Re atom vibrations. Furthermore, four Eg-like modes are observed (identified at 153.6, 163.4, 218.2, and 238.1 cm^{-1}) specific to in-plane Re atom vibrations. The remaining Raman modes possess high frequency and are specific to relatively light S atoms [71]. Thus, one can determine the thickness of few-layer ReS_2 by analyzing the Raman peak positions, much like the approach utilized for MoS_2 [73].

Preprints (www.preprints.org) | NOT PEER-REVIEWED | Posted: 23 August 2021 doi:10.20944/preprints202108.0457.v1

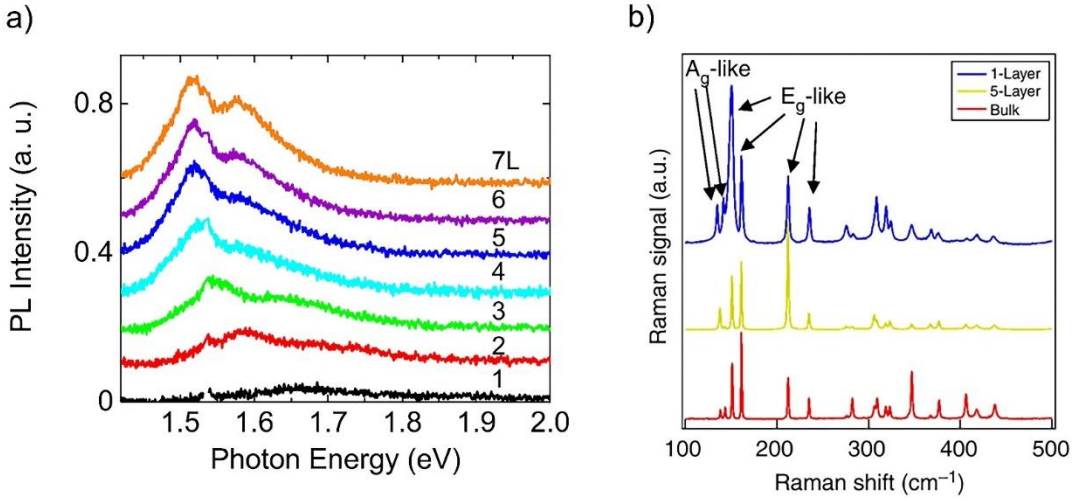

Figure 5. (a) Photoluminescence (PL) spectrum of ReS_2 flakes with different number of layers. Reproduced with permission from Ref. [68]. Copyright 2018, Applied Physics Letters. (b) 18 Raman modes observed on monolayer, five-layer and bulk ReS_2. Six labelled Raman modes include two low frequency Ag-like modes corresponding to the out-of-plane vibrations of Re atoms and four Eg-like modes corresponding to the in-plane vibrations of Re atoms. The rest 12 higher frequency Raman modes are vibrations mainly from lighter S atoms. Reproduced under the terms of a Creative Commons Attribution 4.0 International License [62]. Copyright 2015, Springer Nature.

3. Fabrication and Characterization of ReS_2

The systematic fabrication of 2D ReS_2 with suitable size, thickness, morphology, and crystal quality is substantially important for the exploration of their electronic, optical, and thermal properties for prospective applications. Rhenium (Re) retains one of the highest melting points (~ 3180 °C) among all transition metals whereas disulfide is comparatively low (~ 155 °C). The large difference in melting points makes it considerably challenging to grow ReS_2 thin films. This section summarizes the various fabrication techniques of ReS_2. First part highlights the top-down synthesis approach which comprises of mechanical and liquid phase exfoliations. Subsequent part discusses bottom-up techniques which includes the physical vapor deposition (PVD), chemical vapor transport (CVT), and chemical vapor deposition (CVD) techniques [52]. Depending on the applications' need, various characterizations can be performed for the 2D TMD ReS_2 films. Figure 6 encapsulates the various fabrication and characterization techniques commonly used for 2D TMD ReS_2.

Preprints (www.preprints.org) | NOT PEER-REVIEWED | Posted: 23 August 2021 doi:10.20944/preprints202108.0457.v1

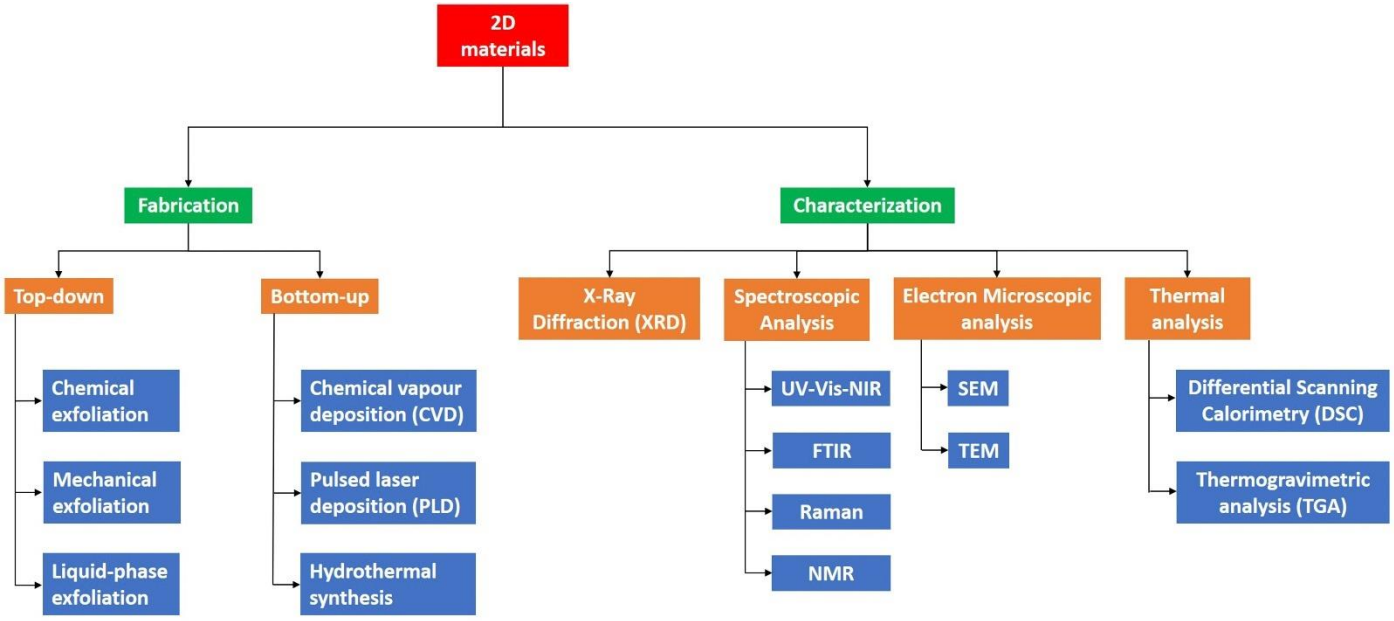

Figure 6. Typical fabrication and characterization methods for 2D TMD materials.

3.1. Top-down Synthesis Techniques

3.1.1. Mechanical Exfoliation

Mechanical exfoliation has an outstanding influence on study and use of 2D materials on their fundamental characteristics. 2D graphene films were first acquired by Novoselov et al. [36] using the scotch tape method scientifically known as the mechanical exfoliation technique. It offers crucial access to high-quality flakes with good mechanical and electrical characteristics in spite of the inexpensive and coarse method [74-77]. A single crystal of bulk material is affixed to the adhesive side of the scotch tape and subsequently an additional piece of tape is positioned on the opposite side of the bulk material. Afterwards, both pieces of tape are peeled for numerous times. A clean and flat substrate, usually SiO_2/Si (300 nm) is then used to affix the freshly sliced thin flake from the scotch tape. Similarly, mono or few layers can be obtained and transferred to the targeted substrate [52]. A highly responsive phototransistors using few layers of ReS_2 is demonstrated by Liu et al. [78] using mechanical exfoliation approach. Figure 7 reveals the usual optical images of $ReSe_2$ and ReS_2 on SiO_2/Si substrate with various layers exfoliated from the bulk materials [79]. However, the shortcomings of this method cannot be overlooked. It may produce edges and ribbons beside crystallographic directions. Also, edges, number of layers and morphology are intense, owing to coarse procedure [80].

Preprints (www.preprints.org) | NOT PEER-REVIEWED | Posted: 23 August 2021 doi:10.20944/preprints202108.0457.v1

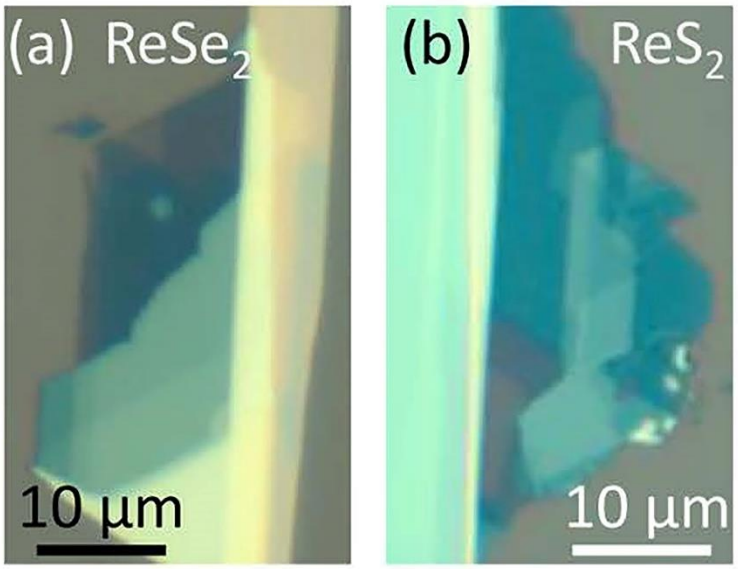

Figure 7. Optical image of a N-layer (a) $ReSe_2$ and (b) ReS_2 crystal. Reproduced with permission from Ref. [79]. Copyright 2016, American Chemical Society.

3.1.2. Liquid Phase Exfoliation

Liquid phase exfoliation is an effective technique for exfoliating ReS_2 nanosheets in large capacity without losing crystal quality. Currently, ReS_2 exfoliation can be classified into two main types; sonication assisted exfoliation and ion intercalation exfoliation [81]. Hersam et. al has reported the ReS_2 exfoliation via layer-by-layer isopycnic density gradient ultracentrifugation sorting of high density nanosheets in aqueous surfactant solutions [81]. At first, ReS_2 powder in deionized water was sonicated with the amphiphilic small molecule surfactant sodium cholate. Subsequently, centrifuged at 7,500 RPM to remove the unexfoliated flakes and the supernatant was collected. To precipitate large size ReS_2 nanosheets, it was further centrifuged at 20,000 RPM. Finally, the comparatively uniform ReS_2 nanosheets were attained with average thickness of around 3 nm and 50–100 nm of lateral size. A mixed solvent strategy was demonstrated using the Hansen solubility theory to prepare few layers of ReS_2 nanosheets by exfoliating bulk ReS_2 in an ethanol-water mixture [82]. It was reported that using a mixture of solvent with 72 % deionized water and 28 % ethanol for sonication is optimum to efficiently exfoliate large scale nanosheets of ReS_2 with an average lateral size of 2.3 nm and a thickness of 50–80 nm. Colloidal ReS_2 nanosheets for antitumor therapy and bioimaging applications using a sonication assisted liquid exfoliation method are also reported by Miao et al. [83].

Another technique to prepare ReS_2 nanosheets is ion intercalation exfoliation. In this method, the cation e.g., Na+, Li+, K+, with small ionic radius can easily insert into the interspace of layered bulk crystals. It expand the interspace drastically and weaken the Van der Waals forces between contiguous layers [52]. Another technique concerning the reaction of ReS_2 powder with lithium borohydride ($LiBH_4$) is developed to replace the conventional protocol requiring butyl lithium solution to effectively exfoliate ReS_2 nanosheets [84]. Nevertheless, the obtained ReS_2 nanosheets with respect to thickness, and lateral size are polydisperse. A homogeneous monolayer ReS_2 film at large scale is challenging. Furthermore, certain solvents and reagents may cause contamination. In this perspective, the nanosheets obtained by this technique are more suited to biological and energy conversion applications [52].

3.2. Bottom-up Synthesis Techniques

3.2.1. Physical Vapor Deposition

Physical vapor deposition (PVD) method is a controlled environmental growth process. The liquid or solid precursors are evaporated in the form of molecules, or atoms in

Preprints (www.preprints.org) | NOT PEER-REVIEWED | Posted: 23 August 2021 doi:10.20944/preprints202108.0457.v1

the presence of a low gas pressure within the high vacuum environment to the targeted substrate [85,86]. Synthesized high quality and large area ReS_2 thin film on top of SiO_2/Si substrate is obtained by using ReS_2 powder (99% pure by Alfa-Aesar) with a cost effective, controlled and simple PVD method as reported by Qi et al. [87]. Before pumping the 1-inch quartz tube to vacuum, ReS_2 powder is placed in the middle of the tube and then filled with argon (Ar) gas as depicted in Figure 8a. The temperature of the furnace is set to 900 °C. After one hour of ReS_2 growth, the furnace is left to naturally cool down. The AFM is used to measure the thickness of ReS_2, and a homogenous film of 2.30 nm thickness (three monolayers) is reported. Subsequently, the crystalline structure and morphology is studies using TEM and SEM, respectively. From the SEM image presented in Figure 8b, the surface of ReS_2 film is found in micrometer size with continuous and clean surface. The as-grown ReS_2 film is observed in nanometer size from the TEM image presented in Figure 8c. The average grain size is reported to be approximately 250 nm and dark-field TEM (DF-TEM) image is revealed in the inset of Figure 8c. However, higher melting point of the precursor and higher vacuum conditions may be the demerits of this technique for possible adaptability [52].

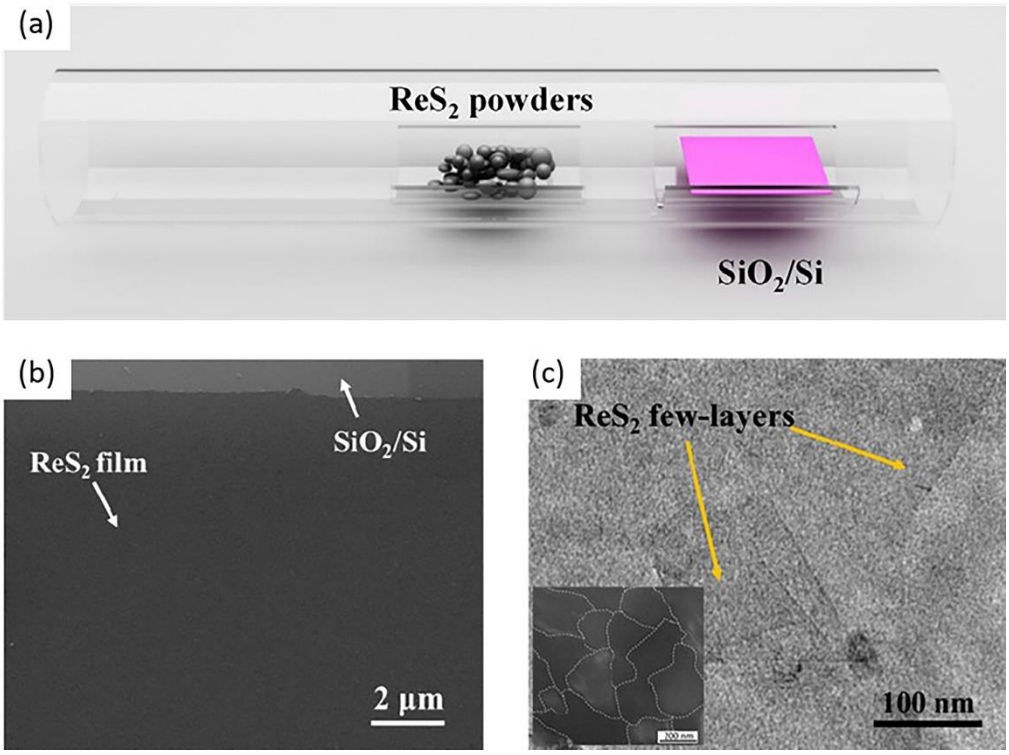

Figure 8. (a) Schematic diagram of synthesized ReS_2 film by PVD. (b) SEM image of ReS_2 film. (c) TEM image of the ReS_2 film. Reproduced with permission from Ref. [87]. Copyright 2016, Elsevier.

3.2.2. Chemical Vapor Transport

Another highly popular approach for synthesis of bulk or single crystals of ReS_2 and $ReSe_2$ is the chemical vapor transport (CVT) technique. In this method, a sealed ampoule tube is used as the growth chamber, the precursor material and transport agent are placed inside the tube for several to ten days under low pressure and high temperature [88]. The halogen (I_2 or Br_2) is used as the transport agent to aid the growth of ReS_2 crystals [61]. Nevertheless, this causes the involuntary background doping and the properties of ReS_2 crystals are also changed [80]. A study reported by Bhakti et al. [89] synthesized high quality ReS_2 and $ReSe_2$ crystals by employing the pure Re and S/Se powders without using halogen transport agent. The growth took place in a cleaned quartz tube at an appropriate temperature using Re and S elements. The shiny plate-like crystals with 20 – 100 microns thickness are witnessed by optical and SEM image as revealed in Figure 9.

Preprints (www.preprints.org) | NOT PEER-REVIEWED | Posted: 23 August 2021 doi:10.20944/preprints202108.0457.v1

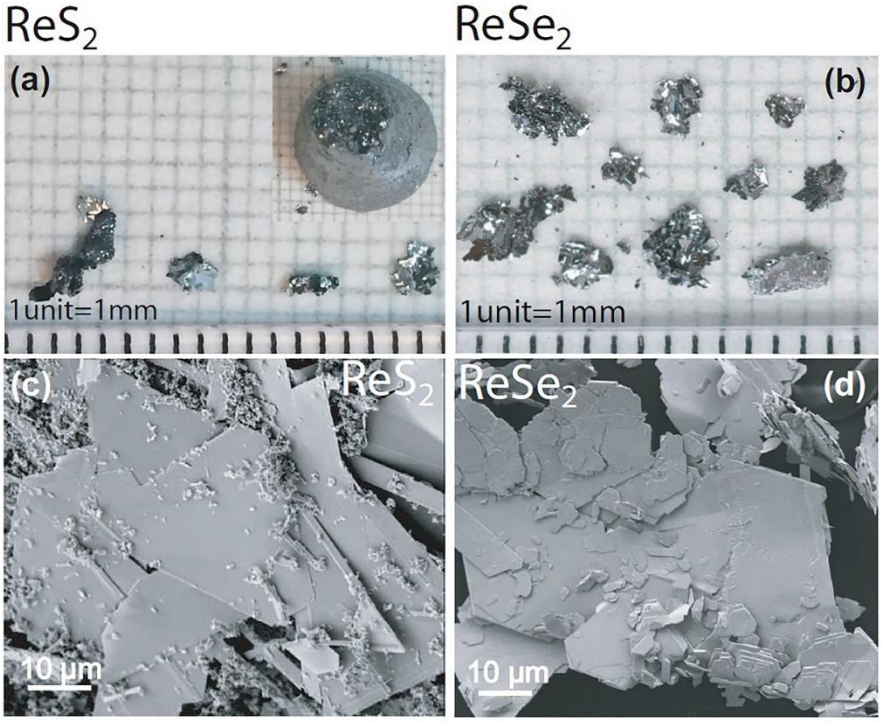

Figure 9. Optical image of the as-grown crystals of (a) ReS_2 (inset shows the ingot as removed from the quartz tube) and (b) $ReSe_2$. SEM images of (c) ReS_2 and (d) $ReSe_2$, showing the surface morphology of the flakes. Reproduced with permission from Ref. [89]. Copyright 2016, American Chemical Society.

Lei Xing et. al has recently developed a new approach by meticulously tuning the growth kinetics for direct synthesizing of thin $ReSe_2$ flakes. The quartz ampoule is specially designed with a neck to separate the powders from the targeted substrate as shown in Figure 10a. This modified method resulted in high quality mono and few layers of $ReSe_2$ nanosheets growth on sapphire or mica substrate as shown in Figure 10b [90].

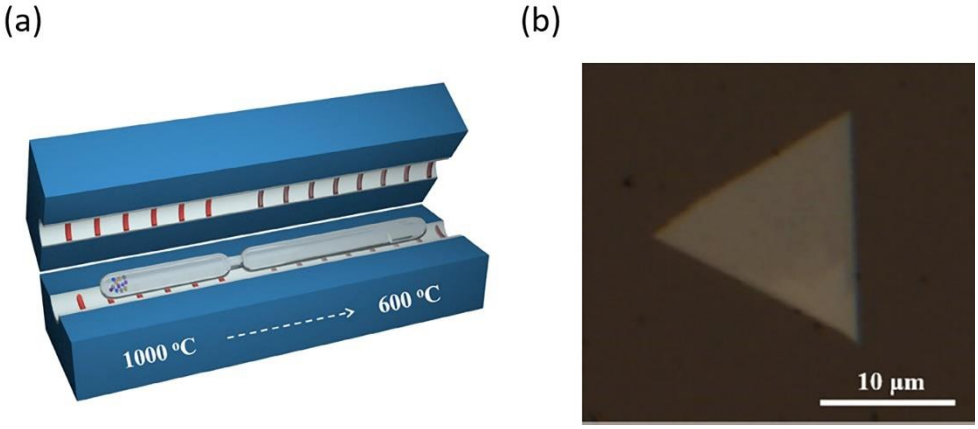

Figure 10. (a) A Schematic for the set-up of CVT growth of ReSe2 flakes. The end of ampoule with the source materials and transport agents is placed at the high temperature zone and the other end is placed at the low temperature zone. (b) Optical image of a typical CVT-grown ReSe2 flake on mica substrate. Reproduced under the terms of a Creative Commons Attribution 4.0 International License [90]. Copyright 2019, John Wiley and Sons.

3.2.3. Chemical Vapor Deposition

Chemical vapor deposition (CVD) technique is intensively employed due to high quality, large area, and uniform films obtained [91,92]. Large-area monolayer ReS_2 thin

Preprints (www.preprints.org) | NOT PEER-REVIEWED | Posted: 23 August 2021 doi:10.20944/preprints202108.0457.v1

films are exhibited by Keyshar et al. [93] recently using scalable CVD synthesis method. Remarkably, low temperature (450 °C) growth is reported for monolayer synthesis compared to previous studies. The uniform polycrystalline bilayer ReS_2 film is obtained by synthesizing hexagonal single crystal flakes of ReS_2 for the first time exploiting CVD method is reported by Hafeez et al. [94]. Three horizontal zones were formed inside the quartz tube within the furnace during the heating process to obtain single and bilayer crystals from the source materials i.e., ReO_3 and sulfur. In another study by Dathbun et al. [95], wafer scale uniform ReS_2 multilayer film is prepared using ReO_3 and H_2S gas as precursor. During the infusion of gas, H_2S directly reacted with ReO_3 and formed ReS_2 film of few cm^2. One of the merits of using this technique is the control on obtained film thickness by regulating the gas flow rate.

4. Saturable Absorbers

4.1. Physics of Saturable Absorption

The absorption basis of 2D layered materials is primarily the Pauli blocking impact [35,96]; this is schematically depicted in Figure 11. When light having photon energy magnitude more than an incident material's bandgap falls on the 2D material surface, valence band electrons are excited to the conduction band due to incident photon absorption (Figure 11a). The hot electrons created are swiftly thermalized to institute a hot Fermi–Dirac dissemination. The thermalized carriers are then cooled down more through the intraband scattering impact (Figure 11b). Next, electron-hole recombination process is active until hole distribution is in equilibrium with electron relaxation. Hence, low transmission is the consequence of a majority of incident photons being absorbed. This phenomenon can be attributed for linear optical photon absorption during relatively weak excitation scenario. During high-intensity incident light conditions, there is a substantial increase in photogenerated carriers; consequently, conduction band states are filled with photon energy up to half of their level. This will impede additional absorption due to the Pauli blocking impact (Figure 11c). Pauli blocking effect indicates that two similar electrons cannot occupy an identical state; consequently, light absorption bleaching occurs (majority of the incident light is not absorbed, causing a high transmission) [35].

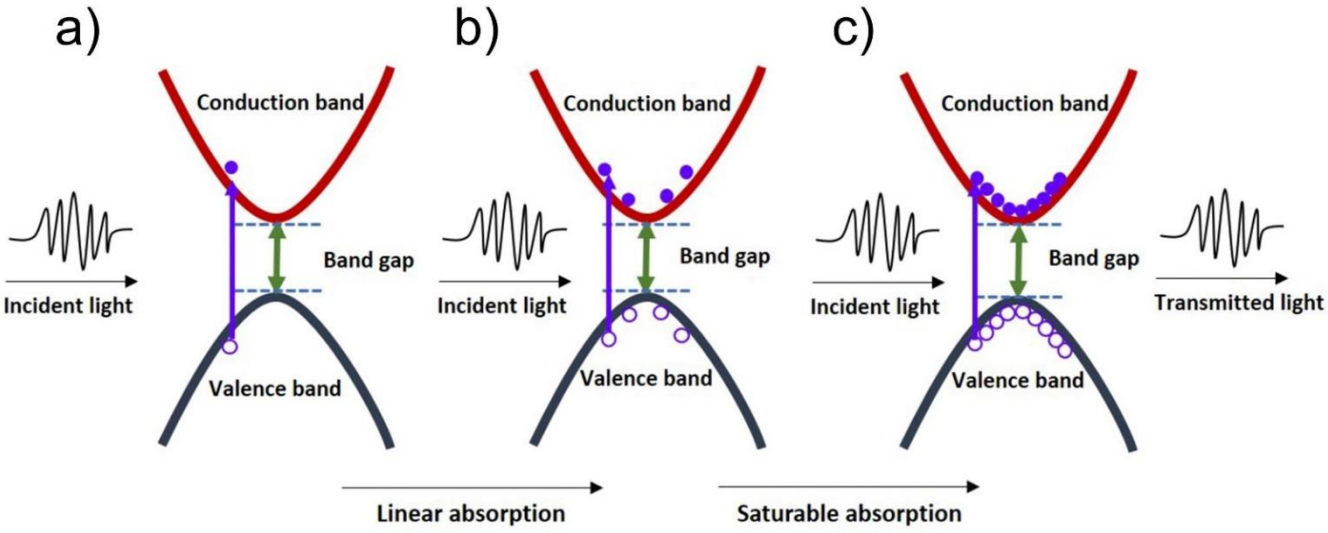

Figure 11. The process of linear absorption and saturable absorption of 2D materials due to Pauli Blocking effect.

4.2. Optical Device Integration and Transfer Strategy

The produced 2D materials are in the form of thin small sheets having nanometer-scale thickness; hence, they cannot be used directly for lasers. Therefore, it is essential to couple materials into proper optical structures to ease the interface between the light and

Preprints (www.preprints.org) | NOT PEER-REVIEWED | Posted: 23 August 2021 doi:10.20944/preprints202108.0457.v1

materials. This type of photonic device having 2D materials utilized in optical fiber or free space structures is known as saturable absorbers (SAs) [58,96]. There are many coupling methods which are summarized in Figure 12. Techniques used for fiber laser applications require material transfer to an end facet of a fiber connector (Figure 12a), tapered fibre (Figure 12b), side-polished fibre (Figure 12c), or filled into the empty photonic crystal fiber (PCF) channels (Figure 12d). It is straightforward and flexible to handle the fiber connector method. A fiber adapter is used to integrate two fibers by placing the SA material in the middle of two end facets. Nevertheless, the obtained material has less damage threshold because SA chemical bonds break due to heat collection due to the high-intensity laser obtained by strong transmission coupling [97]. Side-polished and tapered fiber forms provide the benefit of increased power endurance and damage limits since only a fraction of the light (i.e., evanescent field) interact with the 2D material. Nevertheless, considering that the material has relatively less light intensity, enhancing interaction length can lead to higher non-linearity [98,99]. The PCF scheme is also associated with adequate material-light interaction length and high power-handling ability. In contrast, it is challenging to produce; also, single mode fibers and PCFs have less coupling effectiveness [97]. In the case of solid-state lasers, the coupling schemes are such that there is direct light interaction with the material spin coated on substrates like mirror or quartz glass surface in free-space using reflection or transmission (Figure 12e).

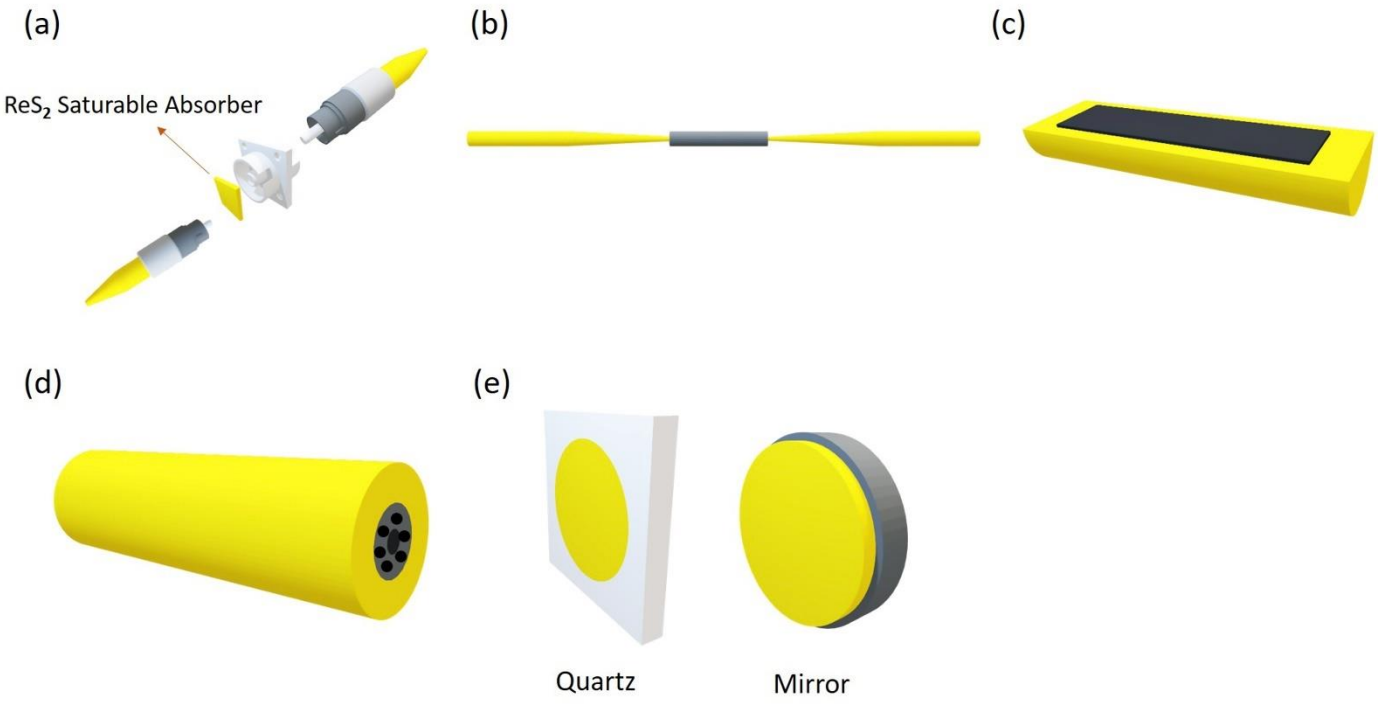

Figure 12. Integration platform for 2D materials to make SA devices. (a) Sandwiched between two fiber connecters using fiber adapter. (b) Tapered fiber. (c) D-shaped (side-polished) fiber. (d) Photonic crystal fiber. (e) Substrate (e.g., quartz glass plate or mirrors) for free-space coupling.

Choosing an appropriate technique for transferring material onto optical devices relies on material production techniques. Considering the mechanical exfoliation method, it is possible to move flake layers to the fiber connector by pressing down the end facet on scotch tape having few-layer thick peeled flakes. Consequently, the adhesive force between the ceramic and flakes causes a 2D-material layer to deposit on the fiber core (Figure 13a) [41]. Optical-driven deposition may be employed for solution-based exfoliation. Initially, the fiber's end facet is dipped inside the solution; subsequently, a strong beam of light is injected. Consequently, the fiber tip gets coated with the material because of temperature-gradient induced material movement [100-102], as depicted in Figure 13b.

Preprints (www.preprints.org) | NOT PEER-REVIEWED | Posted: 23 August 2021 doi:10.20944/preprints202108.0457.v1

Additionally, solution exfoliation nanomaterials can now be transferred using inkjet printing technology. This technique comprises an ink based on 2D flakes; the ink is deposited on the substrate surface, thereby facilitating precisely controlled production at scale [103,104]. Moreover, these nanomaterials may be spread using polymer films like PMMA, PVA, or other substances. Subsequently, the composite layer is placed in the middle of fiber connectors [105].

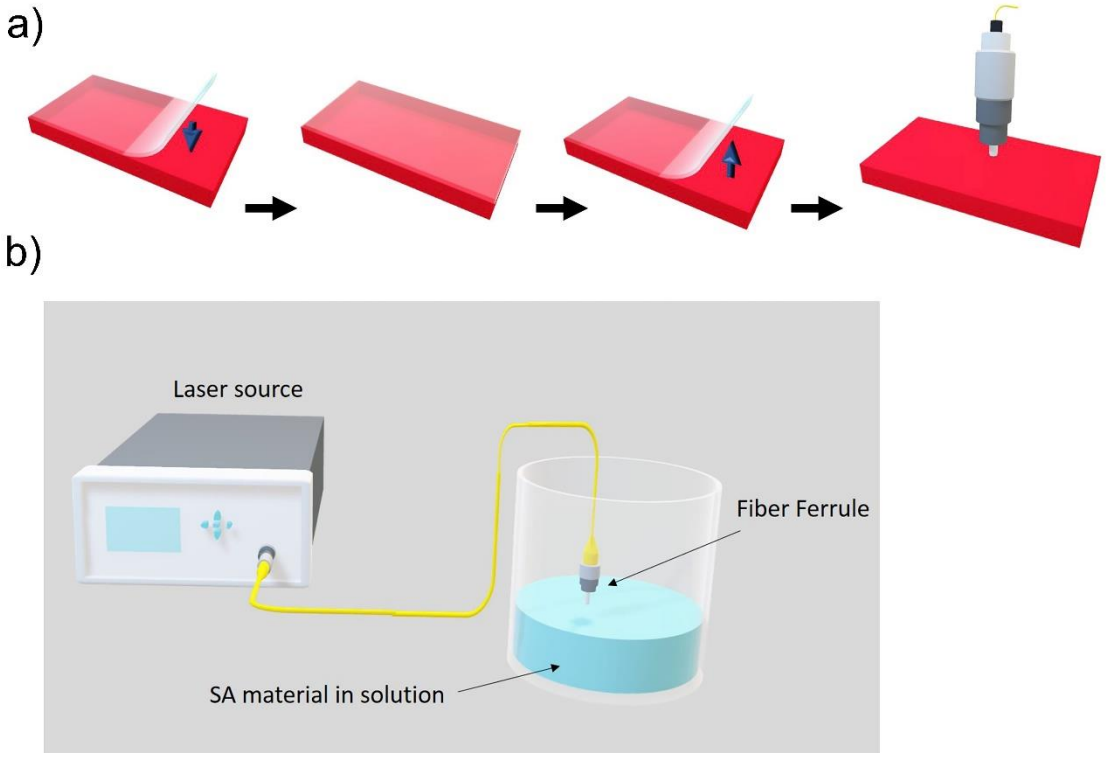

Figure 13. (a) Transferring a mechanically exfoliated few-layer flakes to fiber connecter. (b) Deposition of SA material onto the optical fiber ferrule based on optical driven deposition technique.

4.3. Nonlinear Absorption Characterization

As per the nonlinear optical theory [106], the expression of the absorption of sample could be done based on the relation between the absorption coefficient α and intensity of incident light I as given in Equation (1).

$$\alpha(I) = \alpha_0 + \alpha_{NL} I \quad (1)$$

here, α_0 denotes the linear absorption coefficient and α_{NL} represents the nonlinear absorption coefficient. The expression of nonlinear absorption of SAs could be done as shown in Equation (2) [35,107,108].

$$\alpha(I) = \frac{\alpha_s}{1 + \frac{I}{I_{sat}}} + \alpha_{ns} \quad (2)$$

here, α_s denotes the saturable loss (also called as modulation depth ΔR or ΔT), I_{sat} signifies the saturation intensity and α_{ns} represents the non-saturable loss. Other key parameters pertaining to SAs include the wavelength range (where it absorbs) as well as recovery time τ_A, which need to be of very short time in order to enable passive mode-locking, but not too short with regards to passive Q-switching [109].

For convenience, expression of I can be done as the energy E as well as the incident light's fluence F, thus I_{sat} in Eq. (2) could be replaced by the saturation energy E_{sat} as well as saturation fluence F_{sat} [110]. Various SA parameters with their units and definitions are summarized in Table 1 below:

Preprints (www.preprints.org) | NOT PEER-REVIEWED | Posted: 23 August 2021 doi:10.20944/preprints202108.0457.v1

Table 1. SA parameters, their units, and definitions.

Parameter	Symbol	Unit	Definition
Saturation intensity Saturation energy Saturation fluence	I_{sat} E_{sat} F_{sat}	W/cm^2 J J/cm^2	The required intensity/energy/fluence to reduce absorption by $0.5\alpha_s$
Recovery time	τ_A	S	The decay time of the excitation after an exciting pulse
Modulation depth (also known as saturable loss α_s)	ΔT, ΔR [1] or α_s	in %	Maximum possible change in optical loss $\alpha_s = \alpha_0 - \alpha_{ns}$ [104]
Non-saturable loss	α_{ns} (ΔT_{ns} or ΔR_{ns})	in %	Typically, unwanted part of the losses which cannot be saturated, meaning that the SA device will not reach 100% reflectivity or transmission, even for arbitrarily high pulse intensity [109]

[1] In case the saturable absorber is used in transmission T or reflection R structure.

Two common measurement techniques can be employed to characterize these SA parameters: I-scan measurement (often called as the balanced twin-detector technique) [111] and Z-scan measurement [112]. The Z-scan measurement technique allows characterizing the free-space-type SA sample. As presented in Figure 14a, with the help of a splitter, the pulsed light is first split into two beams of light from the pumping source. The measurement beam would be the beam that propagates along the SA sample's incorporated path, while the other beam would be regarded as the reference beam. The measurement beam is focused by a lens to the SA sample, which has been mounted on a Z-direction translation stage. Changing of light intensity per unit area of the sample can be done based on various beam sizes by moving the sample towards the z-axis along with the measurement beam. The dual-channel power meter is employed to collect the power from both paths. The power from the two detectors is compared in order to obtain the sample's nonlinear absorption. Balanced twin-detector measurement is chosen for SAs that have been integrated as the fiber-based device to perform nonlinear absorption characterization. The principle can be said to be analogous to Z-scan, except that the setup is completely fiberized (Figure 14b). An optical coupler is employed to split the light from a pulsed laser into reference and measurement beams. Unlike the Z-scan method, a variable optical attenuator is mounted before the optical coupler in order to achieve the variation in light intensity for twin-detector measurement [58].

The optical attenuator is employed to change the input power gradually, which enables recording a series of optical transmittance based on different input intensities. Then, characterization and plotting (Figure 14c) of the corresponding nonlinear optical parameters can be done via fitting the relation between the input laser power (I) and the optical transmission rate $T(I)$ based on Equation (3) [98].

$$T(I) = 1 - \Delta T * \exp(-I/I_{sat}) - \alpha_{ns} \quad (3)$$

Preprints (www.preprints.org) | NOT PEER-REVIEWED | Posted: 23 August 2021 doi:10.20944/preprints202108.0457.v1

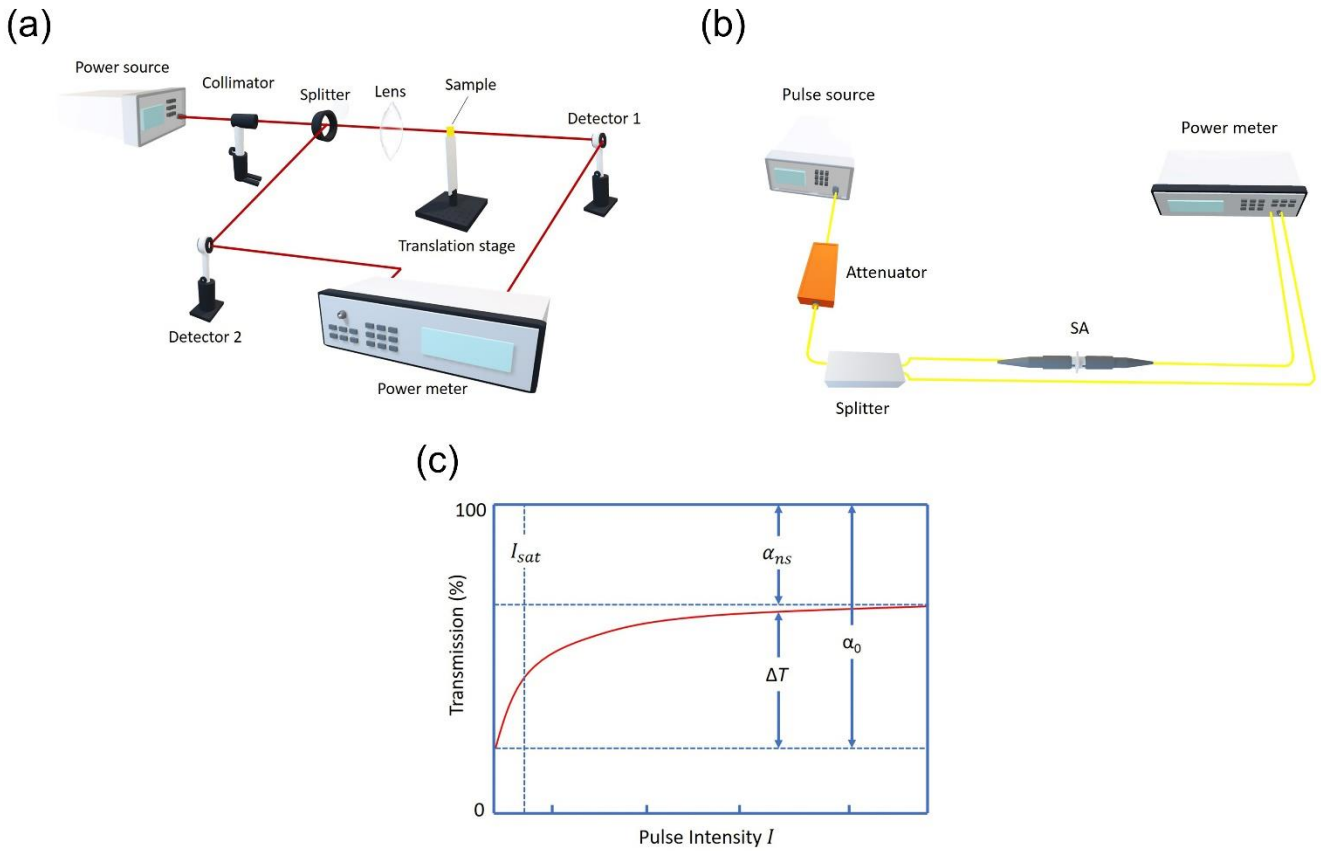

Figure 14. (a) Z-scan measurement (b) I-scan measurement (or balanced twin-detector technique) (c) Example of a transmission curve.

5. Laser Applications Using ReS_2 SA

Based on the operation of Q-switching or mode-locking, integrating SA devices within the laser cavity can aid in creating short optical pulses. Usually, Q-switching can generate pulses possessing high energy (μJ–mJ) at low repetition frequency (kHz) as well as pulse durations in the range of μs–ns. While shorter durations (ps–fs) at higher repetition rate (MHz–GHz) are associated with the mode-locked laser pulses, they also possess lower energy versus Q-switched lasers (pJ–μJ). Both mode-locking and Q-switching can exist together within the same laser cavity but with differing thresholds. Various factors like gain and loss in cavity due to alteration of input power, and balancing between cavity's dispersion and nonlinearity [104] can impact the transition between the two operations. After the first demonstration of pulsed laser by employing ReS_2 as SA with regards to Erbium-doped fiber laser (EDFL) [113], ReS_2-based SA has been employed successfully for various wavelength regions ranging from visible to mid-infrared (0.64-3 μm) in fiber-based as well as solid state laser systems [114-118] leading to several applications as depicted in Figure 15.

Preprints (www.preprints.org) | NOT PEER-REVIEWED | Posted: 23 August 2021 doi:10.20944/preprints202108.0457.v1

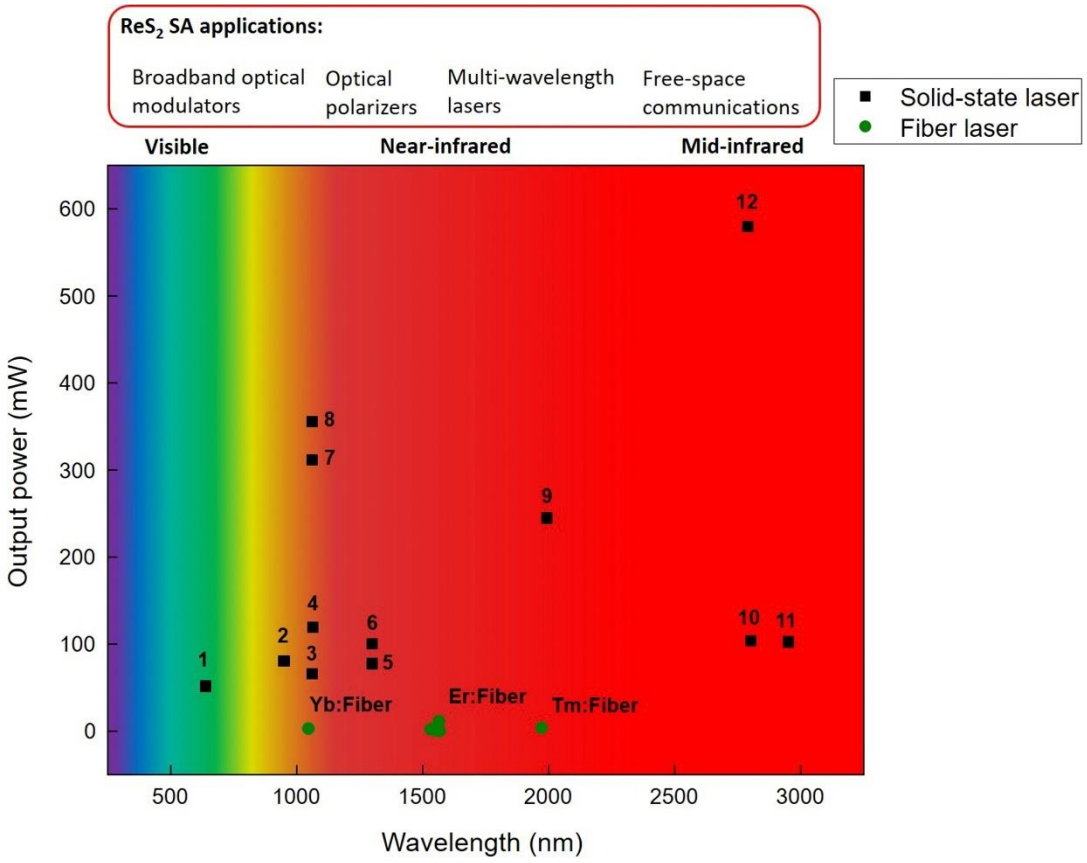

Figure 15. Spectral coverage for several types of pulsed fiber lasers and solid-state lasers generated by ReS_2 SA along with the corresponding output power. 1, Pr:YLF crystal [118]: 2, Nd:YAG crystal [114]: 3, Nd:YAG crystal [119]: 4, Nd:YAG crystal [118]: 5, Nd:YAG crystal [120]: 6, Nd:YAG crystal [119]: 7, Nd:$GdLaNbO_4$ crystal [121]: 8, Nd:YSAG crystal [122]: 9, Tm:YAP crystal [118]: 10, Er:YSGG crystal [123]: 11, Ho,Pr:LLF crystal [117]: 12, Er:SrF2 crystal [124].

5.1. Q-switched Lasers

Typically, Q-switching operation gives pulses possessing higher energy as well as peak power versus mode-locked lasers. Table 2 presents the performance pertaining to Q-switched fiber lasers as well as solid-state lasers with regards to ReS_2-SA. X. Su et al. presented the initial work [123], in which they showed a Q-switched Er:YSGG solid-state pulsed laser at 2.8 μm along with 324 ns pulse duration. Later, various bulk gain medium like Er:SrF2, Pr:YLF, Nd:GdLaNbO4, Tm:YAP and Nd:YAG, were employed, which encompassed broad wavelengths ranging from 640 nm to 2950 nm [117,118]. The ReS_2 was spin-coated on various substrates such as mirror, quartz, sapphire, Yttrium, aluminum garnet (YAG), and K9 glass in order to fabricate the SA device [114,122,124].

With regards to fiber-based laser system, Xu et al. and B. Lu et al. employed Erbium and Ytterbium-doped fibers in order to produce Q-switched laser pulses at 1 μm and 1.5 μm waveband with an average output power of 2.48 mW and 3.2 mW [115,125], respectively. In contrast to fiber lasers, solid-state pulsed lasers offer the benefits of low undesirable nonlinear impacts as well as a wider mode area, which make them optimum for applications that need high power sources [35]. Q-switched solid-state laser possessing maximum average output power of 580 mW as well as highest peak power of 22.1 W was reported by M. Fan et al. who employed Er:SrF_2 crystal as gain medium [124].

Apart from the wide application in infrared lasers, ReS_2-SA is employed for the visible spectrum region. X. Su et al. designed a passively Q-switched laser at 640 nm, which possessed 160 ns pulse duration and 52 mW average output power [118]. Moreover, a Q-switched Nd-doped crystal laser was reported by Han et al. close to ReS_2 bandgap at 950 nm [114]. Various schematic setups are demonstrated in Figure 16 in order to generate Q-

Preprints (www.preprints.org) | NOT PEER-REVIEWED | Posted: 23 August 2021 doi:10.20944/preprints202108.0457.v1

switched lasers based on ReS_2-SA as well as their output characteristics at 1047 nm, 1064 nm, and 1557.3 nm [119,125,126].

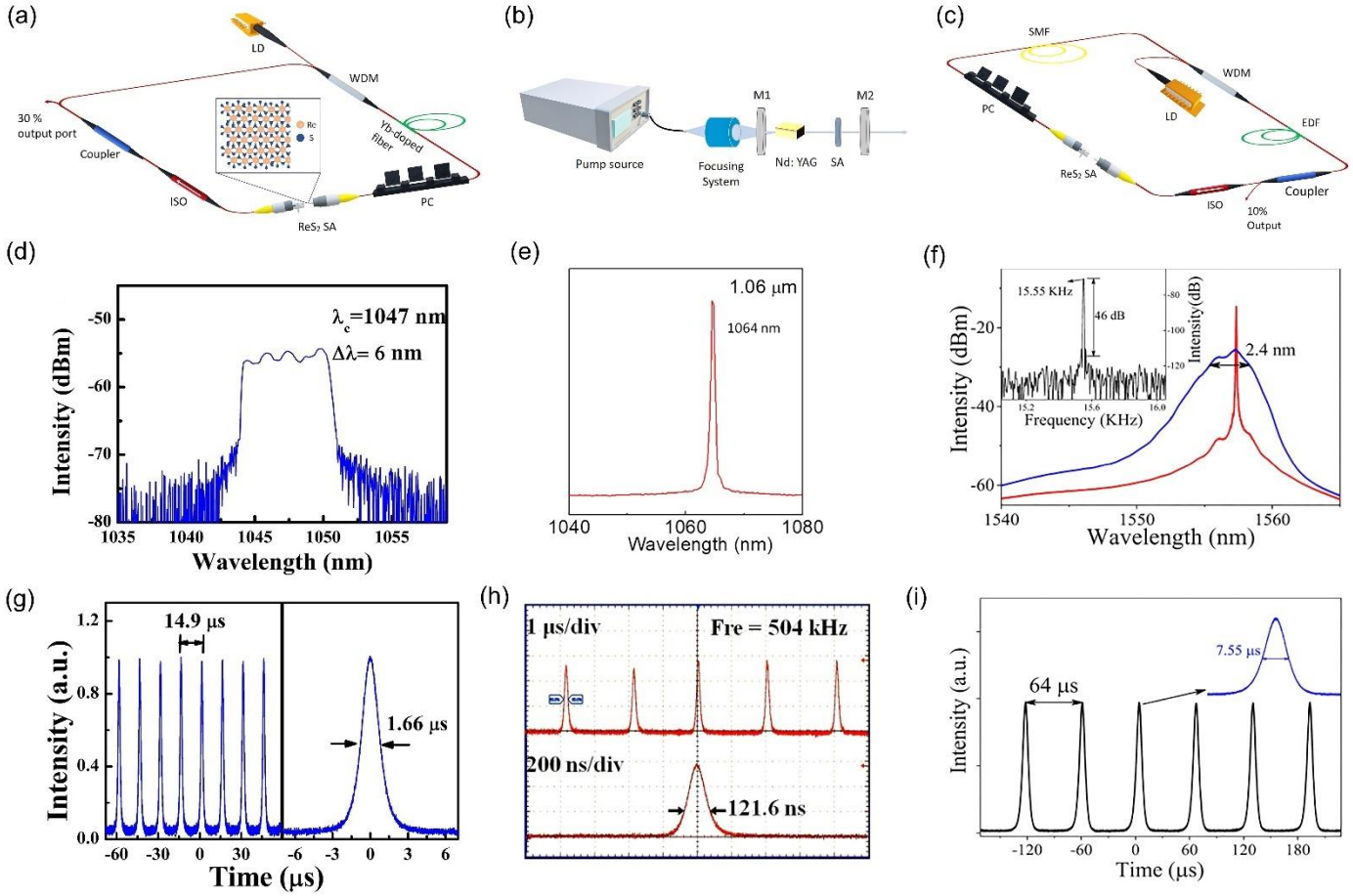

Figure 16. Q-switched pulsed lasers with ReS_2 SA. (a)-(c) cavity designs; (d)-(f) output spectrum; (g)-(i) output pulse trains and the corresponding pulse profile along with the repetition rate and pulse duration. (a) Ref. [125]; adapted with permission; copyright 2018, IEEE. (b) Ref. [119]; adapted with permission; copyright 2019, John Wiley and Sons. (c) Ref. [126]; adapted with permission; copyright 2018, IEEE. (d) and (g), Ref. [125]; reproduced with permission; copyright 2018, IEEE. (e) and (h), Ref. [119]; reproduced with permission; copyright 2019, John Wiley and Sons. (f) and (i), Ref. [126]; reproduced with permission; copyright 2018, IEEE.

Table 2. Nonlinear optical characteristics and applications in laser cavities using ReS_2 for Q-switched lasers. 1

Gain Medium	Fabrication Method	Integration Platform	ReS_2 thickness	Nonlinear characterization		Laser parameters						Ref
				Modulation depth [%]	Saturation level	Wavelength regime (λ_{center})	f_{rep} [kHz]	τ_p [ns]	P_{peak} [W]	E_p [nJ]	P_{out} [mW]	
Yb:Fiber	ME	Fiber connector	21 nm (30 layers)	44	8.4 MW/cm^2	1 μm (1047 nm)	134	1560	0.00813	13.02	3.2	[125]
Er:Fiber	ME	Fiber connector	-	-	150 GW/cm^2	1.5 μm (1532 nm)	64	2100	-	38	2.48	[115]
Er:Fiber	LPE	Fiber connector	~4 nm (6 layers)	0.12	74 MW/cm^2	1.5 μm (1557.3 nm)	19	5496	-	62800	1.2	[126]
Er:Fiber	LPE	Fiber connector	5 nm (7 layers)	-	-	1.5 μm (1550 nm)	66.52	2400	-	18.88	1.25	[127]
Pr:YLF Nd:YAG Tm:YAP crystals	LPE	Mirror	4 nm (6 layers)	3	58.2 μJ/cm^2	Visible (640 nm)	520	160	0.625		52	[118]
				5.2	21.5 μJ/cm^2	1 μm (1064 nm)	644	139	1.34	-	120	
				2.9	2.7 μJ/cm^2	2 μm (1991 nm)	677	415	8.72		245	
Nd:YAG crystal	LPE	Quartz	15 layers	0.33	2.54 GW/cm^2	Visible (946 nm) 1 μm (1064 nm)	165	834	-	491	81	[114]
Nd:$GdLaNbO_4$ crystal	CVD	Sapphire	3.5–5 nm (5–7 layers)	-	-	1 μm (1060 nm)	147	400	5.3	2120	312	[121]
Nd:YSAG crystal	LPS	K9 glass	6 nm	7.4	207.19 MW/cm^2	1 μm (1060 nm)	70	390	-	-	356	[122]
Nd:YAG crystal	LPE	Sapphire	1.4–2 nm (2–3 layers)	2 4	2.17 KW/cm^2 0.55 KW/cm^2	1 μm (1060 nm, 1300 nm)	504 308.4	121.6 111	1.08 2.95	130 330	66 101	[119]
Nd:YAG crystal	LPE	Sapphire	4 nm (6 layers)	15	15.6 μJ/cm^2	1 μm (1300 nm)	214	403	0.9	420	78	[120]

Er:YSGG crystal	LPE	Sapphire	3.5 nm (5 layers)	9.7	22.6 μJ/cm^2	3 μm (2800 nm)	126	324	2.56	825	104	[123]
Er:SrF2 crystal	LPE	Yttrium aluminum garnet (YAG)	2.2 to 7.2 nm (3–10 layers)	3.8	-	3 μm (2790 nm)	49	508	22.1	12100	580	[124]
Ho,Pr:LLF crystal	LPE	Sapphire	4 nm (6 layers)	10.2	23.5 μJ/cm^2	3 μm (2950 nm)	91.5	676	1.67	1130	103	[117]

ME, mechanical exfoliation; LPE, liquid-phase exfoliation; CVD, chemical vapor deposition; LPS, liquid-phase stripping; f_{rep}, repetition frequency; τ_p, pulse duration; P_{peak}, pulse peak power; E_p, pulse energy;P_{out}, output power.

5.2. Mode-Locked Lasers

The performance of mode-locked lasers based on ReS_2 SA is shown in Table 3. As observed, majority of the reports were found to be on near-infrared communication band at 1.5 μm by employing Erbium fiber as gain medium. High quality beam can be produced via fiber lasers platforms along with alignment-free, compact and low-cost structure [30]. In 2017, first identification of mode-locking operation that was based on ReS_2-SA was done [113]. By including the D-shaped fiber possessing ReS_2–polymer composite, generation of mode-locked pulses centered at 1564 nm with pulse duration of 1.25 ps was done as demonstrated in Figure 17a-c. In addition, stable mode-locked pulses at 1563.3 nm possessing pulse width of 3.8 ps was reported by Xu et al. The nature of double covered ReS_2 microfiber structure allowed obtaining high optical damage threshold of 410 mw [65]. Also, a multi-wavelength Er-doped fiber laser (1573.5 nm, 1591.1 nm, and 1592.6 nm) was produced by sandwiching ReS_2 between the two fiber connecters as presented in Figure 17d [128]. Figure 17e displays the output spectrum, which was monitored for about 2 hours to observe long-term stability operation. Similarly, Mao et al. employed a fiber connecter to build a ReS_2-SA device inside the EDFL system, which allowed obtaining self-started mode-locked pulses that were centered at 1558.6 nm along with the duration of 1.6 ps by altering the polarization controller [126]. The first report was realized with regarding mode-locked laser employing ReS_2 in longer wavelengths at 2 μm waveband in thulium-doped fiber laser possessing 893 fs pulse duration as well as 4.13 mw maximum average power [116]. Su et al. employed Yb:CALGO solid-state laser as well as ReS_2 saturable absorption mirror (SAM) to produce 1060 nm mode-locked laser pulses with higher average output power of 350 mW as well as shorter pulse duration of 323 fs [118]. These reports demonstrate that ReS_2 can be employed as broadband SA for various wavelengths, at discrete or multiwavelength operation.

Apart from the broadband saturable absorption, we can also employ large third-order nonlinear effects of ReS_2 to yield pulses possessing high repetition rates with potential applications in frequency combs and soliton communications. Feifei Lu produced pulses with repetition rate, which could reach as high as 318.5 MHz and corresponded to the 168th harmonic mode-locking of Erbium-doped fiber laser [17].

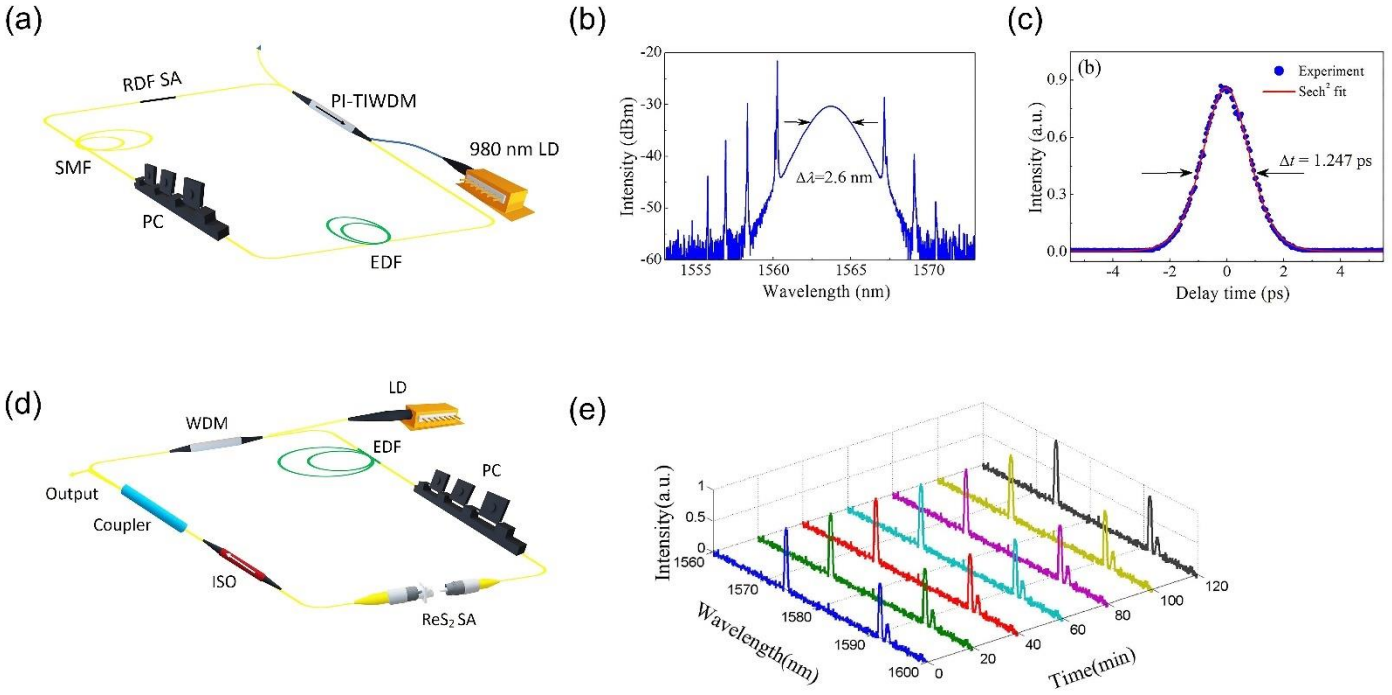

Figure 17. Mode-locked laser pulses at 1.5 μm. (a) Laser setup using ReS_2-covered D-shaped fiber SA (RDF SA). (b) Output optical spectrum with a spectral width Δλ of 2.6 nm. (c) Autocorrelation trace of the experimental data (dots) and $Sech^2$-shaped fit (solid curve) (d) Laser setup with ReS_2

sandwiched between two fiber connectors to form the SA. (e) The corresponding multi-wavelength output with long-term stability over 2 hours. (a) Ref. [113]; adapted under the terms of a Creative Commons Attribution 4.0 International License; copyright 2017, Springer Nature. (b) and (c), Ref. [113]; reproduced under the terms of a Creative Commons Attribution 4.0 International License; copyright 2017, Springer Nature. (d) Ref. [128]; adapted under the terms of a Creative Commons Attribution 4.0 International License; copyright 2018, The Optical Society. (e) Ref. [128]; reproduced under the terms of a Creative Commons Attribution 4.0 International License; copyright 2018, The Optical Society.

Table 3. Nonlinear optical characteristics and applications in laser cavities using ReS_2 for mode-locked lasers

Gain Medium	Fabrication Method	Integration platform	Nonlinear characterization		Laser parameters						Ref
			Modulation depth [%]	Saturation level	Wavelength regime (λ_{center})	Δλ [nm]	f_{rep} [MHz]	τ_p [fs]	P_{out} [mW]	SNR [dB]	
Yb:CALGO crystal	LPE	Mirror	5.2	21.5 μJ/cm^2	1 μm (1060 nm)	4.23	50.7	323	350	60	[118]
Er:Fiber	CVD	D-shaped fiber	1	27 μJ/cm^2	1.5 μm (1564 nm)	2.6	3.43	1250	-	60	[113]
Er:Fiber	CVD	Microfiber	-	-	1.5 μm (1564.4 nm)	0.45	1.896 (318.5 for HML)	2549	12	40	[17]
Er:Fiber	LPE	Fiber connector	6.9	27.5 μJ/cm^2	1.5 μm (1573.6 nm, 1591.1 nm, 1592.6 nm)	17.5	13.39	-	-	55	[128]
Er:Fiber	LPE	Fiber connector	0.12	74 MW/cm^2	1.5 μm (1558.6 nm)	1.85	5.48	1600	0.4	-	[126]
Er:Fiber	LPE	Double-Covered Microfiber	0.25	410 mW	1.5 μm (1563.3 nm)	8.2	1.78	3800	-	68	[65]
Er:Fiber	ME	D-shaped fiber	-	-	1.5 μm (~1560 nm)	15.4	14.53	270	1.08	-	[129]
Er:Fiber	LPE	Microfiber	-	-	1.5 μm (1565 nm)	10.7	20	-	40	80	[130]
Tm:Fiber	Hydrothermal synthesis	Side-polished fiber	62	73.6 W	2 μm (1970.65 nm)	5.05	26.1	893	4.13	70	[116]

Δλ, spectral bandwidth; HML, harmonic mode-locking

5.3. Discussion

The bandgap of ReS_2 amounts to ~1.4 eV which corresponds to an optical absorption at ~800 nm wavelength[131]. Nonetheless, previous works have reported generation of Q-switched and mode-locked lasers using ReS_2 functioning as SA at 1550 nm (~0.8 eV) and 2950 nm (~0.4 eV), which is much less than the bandgap of ReS_2. Thus, in theory, there ought to be no light absorption. Nonetheless, the absorption occurs due to the unavoidable deficiencies in the formation of the material, e.g. grain boundaries and point defects [113]. The introduction of crystallographic or the edge state defect in the material enables the absorption of light photons with energies less than the material bandgap (i.e. sub-bandgap absorption) [132]. By leveraging the effect of sub-bandgap absorption, ReS_2 based SA could consequently support pulsed lasers in the mid-infrared and near-infrared wavelengths where energies of the photons are less than the intended material bandgap. Various theories have been developed to rationalize the sub-bandgap absorption of TMDs, namely decrease in bandgap due to defects [133,134], materials' edge state [135] (can be considered as a special defect at the nanosheets' edges), and saturation of two-photon absorption [136]. X. Su et al. computed the ReS_2 band structure with various ratios of Re and S by using technique of Vienna ab initio simulation, and the results suggest that the bandgap can be decreased from 1.38 to 0.56 eV by introducing S defects in an appropriate range [118]. Moreover, Horzum et al. theoretically examined the atomic imperfections in monolayer ReS_2. It was observed that the S vacancy formation decreases the bandgap from 1.43 to 1.08 eV and the bandgap with Re imperfections becomes only 0.35 eV [137].

The modulation depth, as the main classification parameter of the nonlinear absorption of SA, which is significantly influenced by the material thickness, has a considerable impact on the laser performance. Considerable modulation depth is advantageous for producing short pulses. A concern for monolayer ReS_2-SA (thickness of 0.7 nm [54]) is the low modulation depth that is generally 1% only [113]. By increasing the ReS_2 thickness, the modulation depth can be increased. B. Lu et al. attained up to 44% modulation depth by piling up 30 layers (21 nm) of ReS_2 [125], though this also increases the thresholds of saturation intensity. This is due to the fact that thicker films have higher density of localized defective states on the grain edge and more photons are trapped [65,138]. Intensity/fluence of high saturation implies that the pulsed function can be initiated at higher power level.

Nonetheless, increasing the thickness may have a reverse or positive impact on modulation depth [97]. Mao et al. obtained only 0.12% modulation depth with 6 layers (4 nm) of ReS_2 [126]. ReS_2-SA performance also depends on the wavelength of operation. X. Su et al. demonstrates a reduction in the saturation fluence at higher wavelengths, for instance, 58.2 $\mu J/cm^2$ at 640 nm, 21.5 $\mu J/cm^2$ at 1064 nm, and 2.7 $\mu J/cm^2$ at 1991 nm [118]. This dependence on wavelength makes the use of ReS_2-SA in the mid-infrared region more favorable.

Saturable absorbers having low optical damage threshold can lead to collapse of pulsed operation and instead of that, the laser engages in CW operation, particularly when the material gets deposited on the fiber connector's tip, where the laser connects directly with the material. For instance, pump power above 330 mW caused strong signal jittering to dominate and obliterate the Q-switched pulses [115]; nonetheless, the Q-switched pulses could be obtained again just by reducing the pump power. This is because of the over-saturation of ReS_2-SA instead of thermal damage [139,140]. Many attempts have been carried out to increase the ReS_2-SA damage threshold by utilizing the evanescent field effect through D-shaped or tapered fibers. X. Xu et al. attained stable mode-locking pulses with comparatively high laser damage threshold of 410 mW through double covered ReS_2 micro-fiber as SA device [65].

6. Conclusion and Outlook

In this review, we have emphasized how the property of broadband absorption and large third-order nonlinear effect of ReS_2 can help in development of flexible and low-cost SAs integrated in fiber-based and solid-state lasers. The ReS_2-SA has been effectively used in short pulse generation, providing pulses with maximum peak power up to 22 W, broadband wavelength extending from visible (640 nm) to mid-infrared (2.95 μm) range, and pulse widths down to as low as 270 fs. These outcomes show that ReS_2 is a potential material for several applications like broadband optical modulator, pulsed lasers, and sensors. Majority of the studies utilized liquid-phase exfoliation to form ReS_2. Liquid-phase exfoliation technique is an efficient, convenient, and cheap technique to produce 2D materials. After the process of synthesis, the material is moved to the laser system. Nonetheless, only a fraction of the region of ReS_2 can sustain the Q-switching/mod-locking operation if the material is not distributed entirely and evenly on the integration platform.

A further development for the SAs is to investigate the integration of the emergent ReS_2 with conventional well-established materials like MoS_2 and WS_2. This is likely to help in achieving SAs with greater nonlinearity, higher damage threshold, as well as ultrafast relaxation time by using the properties of various materials. Furthermore, developing hybrid SAs by using artificial SAs like NPE, and real SAs can increase the parameter modulation depth and improve the performance of the output laser. Several applications will be benefited from such ultrafast lasers, and we suppose ReS2 is a potential material for SAs devices. Nonetheless, the most challenging concern is to use these controlled laboratory photonic devices in environmentally stable industrial applications.

Author Contributions: M.M.F drafted the original manuscript; H.R, methodology; N.A supervised and validated the work with the help of other authors. All authors have reviewed and accepted the published version of the manuscript.

Funding: Universiti Kebangsaan Malaysia under Modal Insan funding with grant code MI-2020-002, GUP-2019-010, and Kementerian Sains, Teknologi dan Inovasi (MOSTI) with grant code IF0419IF1082.

Acknowledgments: The authors gratefully acknowledge the financial support of the Department of Electrical, Electronic and Systems Engineering/Faculty of Engineering and Built Environment/Universiti Kebangsaan Malaysia (UKM) for their encouragement and grant support (MI-2020-002, GUP-2019-010, and IF0419IF1082).

Conflicts of Interest: The authors declare no conflicts of interest.

References

1. Keller, U. Recent developments in compact ultrafast lasers. *Nature* **2003**, *424*, 831-838, doi:10.1038/nature01938.
2. Shi, W.; Fang, Q.; Zhu, X.; Norwood, R.A.; Peyghambarian, N. Fiber lasers and their applications. *Appl. Opt.* **2014**, *53*, 6554-6568.
3. Kobayashi, T. Development of ultrashort pulse lasers for ultrafast spectroscopy. *Photonics* **2018**, *5*, 19.
4. Morgenweg, J.; Barmes, I.; Eikema, K.S.E. Ramsey-comb spectroscopy with intense ultrashort laser pulses. *Nat. Phys.* **2014**, *10*, 30-33, doi:10.1038/nphys2807.
5. Udem, T.; Holzwarth, R.; Hänsch, T.W. Optical frequency metrology. *Nature* **2002**, *416*, 233-237, doi:10.1038/416233a.
6. Muhanad Fadhel, M.; Rashid, H.; Essa Hamzah, A.; Dzulkefly Zan, M.S.; Abd Aziz, N.; Arsad, N. Flat frequency comb generation employing cascaded single-drive Mach–Zehnder modulators with a simple analogue driving signal. *J. Mod. Opt.* **2021**, 1-6, doi:10.1080/09500340.2021.1925764.
7. Elgaud, M.M.; Bakar, A.A.A.; Ghaith, A.A.; Naim, N.F.; Arsad, N.; Mokhtar, M.H.H.; Azeman, N.H.; Zan, M.S.D. Pulse Compressed Time Domain Multiplexed Fiber Bragg Grating Sensor: A Comparative Study. *IEEE Access* **2018**, *6*, 64427-64434, doi:10.1109/ACCESS.2018.2877887.

8. Hamzah, A.E.; Zan, M.S.D.; Elgaud, M.; Fadhel, M.M.; Alwash, S.A.; Abushagur, A.A.; Mokhtar, M.H.H.; Azeman, N.H.; Ali, S.H.b.M.; Bakar, A.A.A. Signal Generation using System on Chip for Coded Fiber Bragg Grating Sensor. In Proceedings of the 2020 IEEE 8th International Conference on Photonics (ICP), 12 May-30 June 2020, 2020; pp. 80-81.
9. Zan, M.S.D.; Elgaud, M.M.; Zainuddin, A.R.; Kadhim, A.S.; Mokhtar, M.H.H.; Arsad, N.; Bakar, A.A.A. Simulation Analysis on the Simultaneous Deployment of Brillouin Gain and Loss in Coded Brillouin Optical Time Domain Analysis (BOTDA) Fiber Sensor. *Journal of Physics: Conference Series* **2021**, *1892*, 012034, doi:10.1088/1742-6596/1892/1/012034.
10. Liu, X.; Cui, Y.; Han, D.; Yao, X.; Sun, Z. Distributed ultrafast fibre laser. *Sci. Rep.* **2015**, *5*, 9101, doi:10.1038/srep09101.
11. Taha, B.A.; Ali, N.; Sapiee, N.M.; Fadhel, M.M.; Mat Yeh, R.M.; Bachok, N.N.; Al Mashhadany, Y.; Arsad, N. Comprehensive Review Tapered Optical Fiber Configurations for Sensing Application: Trend and Challenges. *Biosensors* **2021**, *11*, 253.
12. Ippen, E.P. Principles of passive mode locking. *Appl. Phys. B* **1994**, *58*, 159-170.
13. Liu, J.; Wu, J.; Chen, H.; Chen, Y.; Wang, Z.; Ma, C.; Zhang, H. Short-pulsed Raman fiber laser and its dynamics. *SCI CHINA PHYS MECH* **2020**, *64*, 214201, doi:10.1007/s11433-020-1591-2.
14. Haus, H.A. Mode-locking of lasers. *IEEE J. Sel. Top. Quantum Electron.* **2000**, *6*, 1173-1185, doi:10.1109/2944.902165.
15. Xia, W.; Chen, X. Recent developments in fiber-based optical frequency comb and its applications. *Meas. Sci. Technol.* **2016**, *27*, 041001, doi:10.1088/0957-0233/27/4/041001.
16. Woodward, R.I.; Kelleher, E.J. 2D saturable absorbers for fibre lasers. *Appl. Sci.* **2015**, *5*, 1440-1456.
17. Lu, F. Passively harmonic mode-locked fiber laser based on ReS2 saturable absorber. *Mod. Phys. Lett. B* **2017**, *31*, 1750206.
18. Soffer, B.H. Giant Pulse Laser Operation by a Passive, Reversibly Bleachable Absorber. *J. Appl. Phys.* **1964**, *35*, 2551-2551, doi:10.1063/1.1702903.
19. Bret, G.; Gires, F. GIANT-PULSE LASER AND LIGHT AMPLIFIER USING VARIABLE TRANSMISSION COEFFICIENT GLASSES AS LIGHT SWITCHES. *Appl. Phys. Lett.* **1964**, *4*, 175-176, doi:10.1063/1.1753924.
20. Maiman, T.H. Stimulated Optical Radiation in Ruby. *Nature* **1960**, *187*, 493-494, doi:10.1038/187493a0.
21. Ippen, E.P.; Shank, C.V.; Dienes, A. Passive mode locking of the cw dye laser. *Appl. Phys. Lett.* **1972**, *21*, 348-350, doi:10.1063/1.1654406.
22. Dzhibladze, M.I.; Ésiashvili, Z.G.; Teplitskiĭ, É.S.; Isaev, S.K.; Sagaradze, V.R. Mode locking in a fiber laser. *Sov. J. Quantum Electron.* **1983**, *13*, 245-247, doi:10.1070/qe1983v013n02abeh004112.
23. Keller, U.; Miller, D.; Boyd, G.; Chiu, T.; Ferguson, J.; Asom, M. Solid-state low-loss intracavity saturable absorber for Nd: YLF lasers: an antiresonant semiconductor Fabry–Perot saturable absorber. *Opt. Lett.* **1992**, *17*, 505-507.
24. Bogusławski, J.; Wang, Y.; Xue, H.; Yang, X.; Mao, D.; Gan, X.; Ren, Z.; Zhao, J.; Dai, Q.; Soboń, G.; et al. Graphene Actively Mode-Locked Lasers. *Adv. Funct. Mater.* **2018**, *28*, 1801539, doi:https://doi.org/10.1002/adfm.201801539.
25. Wen, Q.-Y.; Tian, W.; Mao, Q.; Chen, Z.; Liu, W.-W.; Yang, Q.-H.; Sanderson, M.; Zhang, H.-W. Graphene based All-Optical Spatial Terahertz Modulator. *Sci. Rep.* **2014**, *4*, 7409, doi:10.1038/srep07409.
26. Zhang, H.; Healy, N.; Shen, L.; Huang, C.C.; Hewak, D.W.; Peacock, A.C. Enhanced all-optical modulation in a graphene-coated fibre with low insertion loss. *Sci. Rep.* **2016**, *6*, 23512, doi:10.1038/srep23512.
27. Cho, B.; Hahm, M.G.; Choi, M.; Yoon, J.; Kim, A.R.; Lee, Y.-J.; Park, S.-G.; Kwon, J.-D.; Kim, C.S.; Song, M.; et al. Charge-transfer-based Gas Sensing Using Atomic-layer MoS2. *Sci. Rep.* **2015**, *5*, 8052, doi:10.1038/srep08052.
28. Wang, S.; Wang, J.; Zhao, W.; Giustiniano, F.; Chu, L.; Verzhbitskiy, I.; Zhou Yong, J.; Eda, G. Efficient Carrier-to-Exciton Conversion in Field Emission Tunnel Diodes Based on MIS-Type van der Waals Heterostack. *Nano Lett.* **2017**, *17*, 5156-5162, doi:10.1021/acs.nanolett.7b02617.
29. Sun, X.; Qiu, C.; Wu, J.; Zhou, H.; Pan, T.; Mao, J.; Yin, X.; Liu, R.; Gao, W.; Fang, Z.; et al. Broadband photodetection in a microfiber-graphene device. *Opt. Express* **2015**, *23*, 25209-25216, doi:10.1364/OE.23.025209.

30. Martinez, A.; Sun, Z. Nanotube and graphene saturable absorbers for fibre lasers. *Nat. Photonics* **2013**, *7*, 842-845, doi:10.1038/nphoton.2013.304.
31. Hu, X.; Yasaei, P.; Jokisaari, J.; Öğüt, S.; Salehi-Khojin, A.; Klie, R.F. Mapping thermal expansion coefficients in freestanding 2D materials at the nanometer scale. *Phys. Rev. Lett.* **2018**, *120*, 055902.
32. Guerreiro, P.T.; Ten, S.; Borrelli, N.F.; Butty, J.; Jabbour, G.E.; Peyghambarian, N. PbS quantum-dot doped glasses as saturable absorbers for mode locking of a Cr:forsterite laser. *Appl. Phys. Lett.* **1997**, *71*, 1595-1597, doi:10.1063/1.119843.
33. Set, S.Y.; Yaguchi, H.; Tanaka, Y.; Jablonski, M. Ultrafast fiber pulsed lasers incorporating carbon nanotubes. *IEEE J. Sel. Top. Quantum Electron.* **2004**, *10*, 137-146, doi:10.1109/JSTQE.2003.822912.
34. Bao, Q.; Zhang, H.; Wang, Y.; Ni, Z.; Yan, Y.; Shen, Z.X.; Loh, K.P.; Tang, D.Y. Atomic-layer graphene as a saturable absorber for ultrafast pulsed lasers. *Adv. Funct. Mater.* **2009**, *19*, 3077-3083.
35. Zhang, B.; Liu, J.; Wang, C.; Yang, K.; Lee, C.; Zhang, H.; He, J. Recent Progress in 2D Material-Based Saturable Absorbers for All Solid-State Pulsed Bulk Lasers. *Laser Photonics Rev.* **2020**, *14*, 1900240, doi:https://doi.org/10.1002/lpor.201900240.
36. Novoselov, K.S.; Geim, A.K.; Morozov, S.V.; Jiang, D.; Zhang, Y.; Dubonos, S.V.; Grigorieva, I.V.; Firsov, A.A. Electric field effect in atomically thin carbon films. *Science* **2004**, *306*, 666-669.
37. Zhao, C.; Zhang, H.; Qi, X.; Chen, Y.; Wang, Z.; Wen, S.; Tang, D. Ultra-short pulse generation by a topological insulator based saturable absorber. *Appl. Phys. Lett.* **2012**, *101*, 211106, doi:10.1063/1.4767919.
38. Salim, M.A.M.; Ab Razak, M.Z.; Azzuhri, S.R.; Ismail, M.A. Generation of Microsecond Ytterbium-Doped Fibre Laser Pulses using Bismuth Telluride Thin Film as Saturable Absorber. *Sains Malays.* **2019**, *48*, 1289-1294.
39. Zhang, H.; Lu, S.; Zheng, J.; Du, J.; Wen, S.; Tang, D.; Loh, K. Molybdenum disulfide (MoS 2) as a broadband saturable absorber for ultra-fast photonics. *Opt. Express* **2014**, *22*, 7249-7260.
40. Aizi Mat Salim, M.; Razalli Azzuhri, S.; Afiq Ismail, M.; Ab. Razak, M.Z. Few Layer Molybdenum Selenide Saturable Absorber using Optical Deposition Technique for Q-switched Ytterbium Pulses Laser Generation. *Journal of Physics: Conference Series* **2020**, *1484*, 012025, doi:10.1088/1742-6596/1484/1/012025.
41. Chen, Y.; Jiang, G.; Chen, S.; Guo, Z.; Yu, X.; Zhao, C.; Zhang, H.; Bao, Q.; Wen, S.; Tang, D. Mechanically exfoliated black phosphorus as a new saturable absorber for both Q-switching and mode-locking laser operation. *Opt. Express* **2015**, *23*, 12823-12833.
42. Sotor, J.; Sobon, G.; Macherzynski, W.; Paletko, P.; Abramski, K.M. Black phosphorus saturable absorber for ultrashort pulse generation. *Appl. Phys. Lett.* **2015**, *107*, 051108, doi:10.1063/1.4927673.
43. Jhon, Y.I.; Koo, J.; Anasori, B.; Seo, M.; Lee, J.H.; Gogotsi, Y.; Jhon, Y.M. Metallic MXene saturable absorber for femtosecond mode-locked lasers. *Adv. Mater.* **2017**, *29*, 1702496.
44. Song, Y.; Liang, Z.; Jiang, X.; Chen, Y.; Li, Z.; Lu, L.; Ge, Y.; Wang, K.; Zheng, J.; Lu, S.; et al. Few-layer antimonene decorated microfiber: ultra-short pulse generation and all-optical thresholding with enhanced long term stability. *2D Mater.* **2017**, *4*, 045010, doi:10.1088/2053-1583/aa87c1.
45. Hu, P.; Liu, Y.; Guo, L.; Ge, X.; Liu, X.; Yu, L.; Liu, Q. Passively Q-switched erbium-doped fiber laser based on antimonene as saturable absorber. *Appl. Opt.* **2019**, *58*, 7845-7850, doi:10.1364/AO.58.007845.
46. Lu, L.; Liang, Z.; Wu, L.; Chen, Y.; Song, Y.; Dhanabalan, S.C.; Ponraj, J.S.; Dong, B.; Xiang, Y.; Xing, F.; et al. Few-layer Bismuthene: Sonochemical Exfoliation, Nonlinear Optics and Applications for Ultrafast Photonics with Enhanced Stability. *Laser Photonics Rev.* **2018**, *12*, 1700221, doi:https://doi.org/10.1002/lpor.201700221.
47. Chai, T.; Li, X.; Feng, T.; Guo, P.; Song, Y.; Chen, Y.; Zhang, H. Few-layer bismuthene for ultrashort pulse generation in a dissipative system based on an evanescent field. *Nanoscale* **2018**, *10*, 17617-17622, doi:10.1039/C8NR03068E.

48. Guo, B.; Wang, S.-H.; Wu, Z.-X.; Wang, Z.-X.; Wang, D.-H.; Huang, H.; Zhang, F.; Ge, Y.-Q.; Zhang, H. Sub-200 fs soliton mode-locked fiber laser based on bismuthene saturable absorber. *Opt. Express* **2018**, *26*, 22750-22760, doi:10.1364/OE.26.022750.
49. Ma, X.; Zhang, Z.; Jiang, W.; Tong, L.; Liu, S.; Dai, W.; Chen, W.; Zhou, Y.; Zhang, W.; Qiu, J.; et al. Passively mode-locked thulium doped fiber laser based on SnSe nanoparticles as a saturable absorber. *Opt. Laser Technol.* **2021**, *138*, 106870, doi:https://doi.org/10.1016/j.optlastec.2020.106870.
50. Chhowalla, M.; Shin, H.S.; Eda, G.; Li, L.-J.; Loh, K.P.; Zhang, H. The chemistry of two-dimensional layered transition metal dichalcogenide nanosheets. *Nat. Chem.* **2013**, *5*, 263-275, doi:10.1038/nchem.1589.
51. Wilson, J.A.; Yoffe, A. The transition metal dichalcogenides discussion and interpretation of the observed optical, electrical and structural properties. *Adv. Phys.* **1969**, *18*, 193-335.
52. Li, X.; Chen, C.; Yang, Y.; Lei, Z.; Xu, H. 2D Re-Based Transition Metal Chalcogenides: Progress, Challenges, and Opportunities. *Adv. Sci.* **2020**, 2002320.
53. Rahman, M.; Davey, K.; Qiao, S.Z. Advent of 2D rhenium disulfide (ReS2): fundamentals to applications. *Adv. Funct. Mater.* **2017**, *27*, 1606129.
54. Tongay, S.; Sahin, H.; Ko, C.; Luce, A.; Fan, W.; Liu, K.; Zhou, J.; Huang, Y.-S.; Ho, C.-H.; Yan, J.; et al. Monolayer behaviour in bulk ReS2 due to electronic and vibrational decoupling. *Nat. Commun.* **2014**, *5*, 3252, doi:10.1038/ncomms4252.
55. Zhang, Q.; Fu, L. Novel Insights and Perspectives into Weakly Coupled ReS2 toward Emerging Applications. *Chem* **2019**, *5*, 505-525, doi:https://doi.org/10.1016/j.chempr.2018.11.004.
56. Zhang, E.; Jin, Y.; Yuan, X.; Wang, W.; Zhang, C.; Tang, L.; Liu, S.; Zhou, P.; Hu, W.; Xiu, F. ReS2-Based Field-Effect Transistors and Photodetectors. *Adv. Funct. Mater.* **2015**, *25*, 4076-4082.
57. Zulkefli, A.; Mukherjee, B.; Iwasaki, T.; Hayakawa, R.; Nakaharai, S.; Wakayama, Y. Gate-bias tunable humidity sensors based on rhenium disulfide field-effect transistors. *Jpn. J. Appl. Phys.* **2020**, *60*, SBBH01, doi:10.35848/1347-4065/abd2a0.
58. Hao, Q.; Wang, C.; Liu, W.; Liu, X.; Liu, J.; Zhang, H. Low-dimensional saturable absorbers for ultrafast photonics in solid-state bulk lasers: status and prospects. *Nanophotonics* **2020**, *9*, 2603-2639, doi:https://doi.org/10.1515/nanoph-2019-0544.
59. Liu, X.; Gao, Q.; Zheng, Y.; Mao, D.; Zhao, J. Recent progress of pulsed fiber lasers based on transition-metal dichalcogenides and black phosphorus saturable absorbers. *Nanophotonics* **2020**, *9*, 2215-2231, doi:https://doi.org/10.1515/nanoph-2019-0566.
60. Noddack, W. Die ekamangane. *Naturwissenschaften* **1925**, *13*, 567.
61. Lin, Y.-C.; Komsa, H.-P.; Yeh, C.-H.; Bjorkman, T.; Liang, Z.-Y.; Ho, C.-H.; Huang, Y.-S.; Chiu, P.-W.; Krasheninnikov, A.V.; Suenaga, K. Single-layer ReS2: two-dimensional semiconductor with tunable in-plane anisotropy. *ACS Nano* **2015**, *9*, 11249-11257.
62. Liu, E.; Fu, Y.; Wang, Y.; Feng, Y.; Liu, H.; Wan, X.; Zhou, W.; Wang, B.; Shao, L.; Ho, C.-H.; et al. Integrated digital inverters based on two-dimensional anisotropic ReS2 field-effect transistors. *Nat. Commun.* **2015**, *6*, 6991, doi:10.1038/ncomms7991.
63. Yun, W.S.; Han, S.; Hong, S.C.; Kim, I.G.; Lee, J. Thickness and strain effects on electronic structures of transition metal dichalcogenides: 2H-M X 2 semiconductors (M= Mo, W; X= S, Se, Te). *Phys. Rev. B* **2012**, *85*, 033305.
64. Zhang, H.; Li, X.-B.; Liu, L.-M. Tunable electronic and magnetic properties of WS2 nanoribbons. *J. Appl. Phys.* **2013**, *114*, 093710, doi:10.1063/1.4820470.
65. Xu, X.; He, M.; Quan, C.; Wang, R.; Liu, C.; Zhao, Q.; Zhou, Y.; Bai, J.; Xu, X. Saturable Absorption Properties of ReS2 Films and Mode-Locking Application Based on Double-Covered ReS2 Micro Fiber. *J. Light. Technol.* **2018**, *36*, 5130-5136, doi:10.1109/JLT.2018.2870433.
66. Ho, C.; Huang, Y.; Tiong, K.; Liao, P. In-plane anisotropy of the optical and electrical properties of layered ReS2 crystals. *J. Phys. Condens. Matter* **1999**, *11*, 5367.

67. Liu, S.; Wang, M.; Yin, S.; Xie, Z.; Wang, Z.; Zhou, S.; Chen, P. Nonlinear Optical Properties of Few-Layer Rhenium Disulfide Nanosheets and Their Passively Q-switched Laser Application. *Phys. Status Solidi A* **2019**, *216*, 1800837, doi:https://doi.org/10.1002/pssa.201800837.
68. Mohamed, N.B.; Shinokita, K.; Wang, X.; Lim, H.E.; Tan, D.; Miyauchi, Y.; Matsuda, K. Photoluminescence quantum yields for atomically thin-layered ReS2: Identification of indirect-bandgap semiconductors. *Appl. Phys. Lett.* **2018**, *113*, 121112, doi:10.1063/1.5037116.
69. Li, X.; Chen, C.; Yang, Y.; Lei, Z.; Xu, H. 2D Re-Based Transition Metal Chalcogenides: Progress, Challenges, and Opportunities. *Adv. Sci.* **2020**, *7*, 2002320, doi:https://doi.org/10.1002/advs.202002320.
70. Chenet, D.A.; Aslan, O.B.; Huang, P.Y.; Fan, C.; van der Zande, A.M.; Heinz, T.F.; Hone, J.C. In-Plane Anisotropy in Mono- and Few-Layer ReS2 Probed by Raman Spectroscopy and Scanning Transmission Electron Microscopy. *Nano Lett.* **2015**, *15*, 5667-5672, doi:10.1021/acs.nanolett.5b00910.
71. Feng, Y.; Zhou, W.; Wang, Y.; Zhou, J.; Liu, E.; Fu, Y.; Ni, Z.; Wu, X.; Yuan, H.; Miao, F.; et al. Raman vibrational spectra of bulk to monolayer ReS2 with lower symmetry. *Phys. Rev. B* **2015**, *92*, 054110, doi:10.1103/PhysRevB.92.054110.
72. Nagler, P.; Plechinger, G.; Schüller, C.; Korn, T. Observation of anisotropic interlayer Raman modes in few-layer ReS2. *Phys. Status Solidi RRL* **2016**, *10*, 185-189, doi:https://doi.org/10.1002/pssr.201510412.
73. Lee, C.; Yan, H.; Brus, L.E.; Heinz, T.F.; Hone, J.; Ryu, S. Anomalous Lattice Vibrations of Single- and Few-Layer MoS2. *ACS Nano* **2010**, *4*, 2695-2700, doi:10.1021/nn1003937.
74. Lee, C.; Wei, X.; Kysar, J.W.; Hone, J. Measurement of the elastic properties and intrinsic strength of monolayer graphene. *Science* **2008**, *321*, 385-388.
75. Bertolazzi, S.; Brivio, J.; Kis, A. Stretching and Breaking of Ultrathin MoS2. *ACS Nano* **2011**, *5*, 9703-9709, doi:10.1021/nn203879f.
76. Novoselov, K.S.; Geim, A.K.; Morozov, S.V.; Jiang, D.; Katsnelson, M.I.; Grigorieva, I.V.; Dubonos, S.V.; Firsov, A.A. Two-dimensional gas of massless Dirac fermions in graphene. *Nature* **2005**, *438*, 197-200, doi:10.1038/nature04233.
77. Zhang, Y.; Tan, Y.-W.; Stormer, H.L.; Kim, P. Experimental observation of the quantum Hall effect and Berry's phase in graphene. *Nature* **2005**, *438*, 201-204, doi:10.1038/nature04235.
78. Liu, E.; Long, M.; Zeng, J.; Luo, W.; Wang, Y.; Pan, Y.; Zhou, W.; Wang, B.; Hu, W.; Ni, Z. High responsivity phototransistors based on few-layer ReS2 for weak signal detection. *Adv. Funct. Mater.* **2016**, *26*, 1938-1944.
79. Lorchat, E.; Froehlicher, G.; Berciaud, S. Splitting of Interlayer Shear Modes and Photon Energy Dependent Anisotropic Raman Response in N-Layer ReSe2 and ReS2. *ACS Nano* **2016**, *10*, 2752-2760, doi:10.1021/acsnano.5b07844.
80. Xiong, Y.; Chen, H.; Zhang, D.W.; Zhou, P. Electronic and optoelectronic applications based on ReS2. *physica status solidi (RRL)–Rapid Research Letters* **2019**, *13*, 1800658.
81. Kang, J.; Sangwan, V.K.; Wood, J.D.; Liu, X.; Balla, I.; Lam, D.; Hersam, M.C. Layer-by-Layer Sorting of Rhenium Disulfide via High-Density Isopycnic Density Gradient Ultracentrifugation. *Nano Lett.* **2016**, *16*, 7216-7223, doi:10.1021/acs.nanolett.6b03584.
82. Xu, X.; Guo, Y.; Zhao, Q.; Si, K.; Zhou, Y.; Ma, J.; Bai, J.; Xu, X. Green and efficient exfoliation of ReS2 and its photoelectric response based on electrophoretic deposited photoelectrodes. *Materials & Design* **2018**, *159*, 11-19.
83. Miao, Z.H.; Lv, L.X.; Li, K.; Liu, P.Y.; Li, Z.; Yang, H.; Zhao, Q.; Chang, M.; Zhen, L.; Xu, C.Y. Liquid exfoliation of colloidal rhenium disulfide nanosheets as a multifunctional theranostic agent for in vivo photoacoustic/ct imaging and photothermal therapy. *Small* **2018**, *14*, 1703789.
84. Fujita, T.; Ito, Y.; Tan, Y.; Yamaguchi, H.; Hojo, D.; Hirata, A.; Voiry, D.; Chhowalla, M.; Chen, M. Chemically exfoliated ReS2 nanosheets. *Nanoscale* **2014**, *6*, 12458-12462, doi:10.1039/C4NR03740E.

85. Wu, S.; Huang, C.; Aivazian, G.; Ross, J.S.; Cobden, D.H.; Xu, X. Vapor–solid growth of high optical quality MoS2 monolayers with near-unity valley polarization. *ACS Nano* **2013**, *7*, 2768-2772.
86. Feng, Q.; Zhu, Y.; Hong, J.; Zhang, M.; Duan, W.; Mao, N.; Wu, J.; Xu, H.; Dong, F.; Lin, F.; et al. Growth of Large-Area 2D MoS2(1-x)Se2x Semiconductor Alloys. *Adv. Mater.* **2014**, *26*, 2648-2653, doi:https://doi.org/10.1002/adma.201306095.
87. Qi, F.; Chen, Y.; Zheng, B.; Zhou, J.; Wang, X.; Li, P.; Zhang, W. Facile growth of large-area and high-quality few-layer ReS2 by physical vapour deposition. *Materials Letters* **2016**, *184*, 324-327.
88. Wang, D.; Luo, F.; Lu, M.; Xie, X.; Huang, L.; Huang, W. Chemical Vapor Transport Reactions for Synthesizing Layered Materials and Their 2D Counterparts. *Small* **2019**, *15*, 1804404, doi:https://doi.org/10.1002/smll.201804404.
89. Jariwala, B.; Voiry, D.; Jindal, A.; Chalke, B.A.; Bapat, R.; Thamizhavel, A.; Chhowalla, M.; Deshmukh, M.; Bhattacharya, A. Synthesis and Characterization of ReS2 and ReSe2 Layered Chalcogenide Single Crystals. *Chemistry of Materials* **2016**, *28*, 3352-3359, doi:10.1021/acs.chemmater.6b00364.
90. Xing, L.; Yan, X.; Zheng, J.; Xu, G.; Lu, Z.; Liu, L.; Wang, J.; Wang, P.; Pan, X.; Jiao, L. Highly crystalline ReSe2 atomic layers synthesized by chemical vapor transport. *InfoMat* **2019**, *1*, 552-558, doi:https://doi.org/10.1002/inf2.12041.
91. Zhou, X.; Gan, L.; Tian, W.; Zhang, Q.; Jin, S.; Li, H.; Bando, Y.; Golberg, D.; Zhai, T. Ultrathin SnSe2 Flakes Grown by Chemical Vapor Deposition for High-Performance Photodetectors. *Adv. Mater.* **2015**, *27*, 8035-8041, doi:https://doi.org/10.1002/adma.201503873.
92. Lee, Y.-H.; Zhang, X.-Q.; Zhang, W.; Chang, M.-T.; Lin, C.-T.; Chang, K.-D.; Yu, Y.-C.; Wang, J.T.-W.; Chang, C.-S.; Li, L.-J.; et al. Synthesis of Large-Area MoS2 Atomic Layers with Chemical Vapor Deposition. *Adv. Mater.* **2012**, *24*, 2320-2325, doi:https://doi.org/10.1002/adma.201104798.
93. Keyshar, K.; Gong, Y.; Ye, G.; Brunetto, G.; Zhou, W.; Cole, D.P.; Hackenberg, K.; He, Y.; Machado, L.; Kabbani, M. Chemical vapor deposition of monolayer rhenium disulfide (ReS2). *Adv. Mater.* **2015**, *27*, 4640-4648.
94. Hafeez, M.; Gan, L.; Li, H.; Ma, Y.; Zhai, T. Large-area bilayer ReS2 film/multilayer ReS2 flakes synthesized by chemical vapor deposition for high performance photodetectors. *Adv. Funct. Mater.* **2016**, *26*, 4551-4560.
95. Dathbun, A.; Kim, Y.; Kim, S.; Yoo, Y.; Kang, M.S.; Lee, C.; Cho, J.H. Large-Area CVD-Grown Sub-2 V ReS2 Transistors and Logic Gates. *Nano Lett.* **2017**, *17*, 2999-3005, doi:10.1021/acs.nanolett.7b00315.
96. Wang, G.; Baker-Murray, A.A.; Blau, W.J. Saturable Absorption in 2D Nanomaterials and Related Photonic Devices. *Laser Photonics Rev.* **2019**, *13*, 1800282, doi:https://doi.org/10.1002/lpor.201800282.
97. Liu, W.; Liu, M.; Liu, X.; Wang, X.; Deng, H.X.; Lei, M.; Wei, Z.; Wei, Z. Recent advances of 2D materials in nonlinear photonics and fiber lasers. *Adv. Opt. Mater.* **2020**, *8*, 1901631.
98. Du, J.; Wang, Q.; Jiang, G.; Xu, C.; Zhao, C.; Xiang, Y.; Chen, Y.; Wen, S.; Zhang, H. Ytterbium-doped fiber laser passively mode locked by few-layer Molybdenum Disulfide (MoS2) saturable absorber functioned with evanescent field interaction. *Sci. Rep.* **2014**, *4*, 6346, doi:10.1038/srep06346.
99. Song, Y.-W.; Yamashita, S.; Maruyama, S. Single-walled carbon nanotubes for high-energy optical pulse formation. *Appl. Phys. Lett.* **2008**, *92*, 021115, doi:10.1063/1.2834898.
100. Ge, Y.; Zhu, Z.; Xu, Y.; Chen, Y.; Chen, S.; Liang, Z.; Song, Y.; Zou, Y.; Zeng, H.; Xu, S.; et al. Broadband Nonlinear Photoresponse of 2D TiS2 for Ultrashort Pulse Generation and All-Optical Thresholding Devices. *Adv. Opt. Mater.* **2018**, *6*, 1701166, doi:https://doi.org/10.1002/adom.201701166.
101. Khazaeinezhad, R.; Hosseinzadeh Kassani, S.; Nazari, T.; Jeong, H.; Kim, J.; Choi, K.; Lee, J.-U.; Kim, J.H.; Cheong, H.; Yeom, D.-I.; et al. Saturable optical absorption in MoS2 nano-sheet optically deposited on the optical fiber facet. *Opt. Commun.* **2015**, *335*, 224-230, doi:https://doi.org/10.1016/j.optcom.2014.09.038.
102. Ahmad, H.; Muhammad, F.D.; Zulkifli, M.Z.; Harun, S.W. Graphene-Oxide-Based Saturable Absorber for All-Fiber Q-Switching With a Simple Optical Deposition Technique. *IEEE Photon. J.* **2012**, *4*, 2205-2213, doi:10.1109/JPHOT.2012.2228478.

103. Jin, X.; Hu, G.; Zhang, M.; Hu, Y.; Albrow-Owen, T.; Howe, R.C.; Wu, T.-C.; Wu, Q.; Zheng, Z.; Hasan, T. 102 fs pulse generation from a long-term stable, inkjet-printed black phosphorus-mode-locked fiber laser. *Opt. Express* **2018**, *26*, 12506-12513.

104. Zhang, M.; Wu, Q.; Zhang, F.; Chen, L.; Jin, X.; Hu, Y.; Zheng, Z.; Zhang, H. 2D Black Phosphorus Saturable Absorbers for Ultrafast Photonics. *Adv. Opt. Mater.* **2019**, *7*, 1800224, doi:https://doi.org/10.1002/adom.201800224.

105. Mao, D.; Li, M.; Cui, X.; Zhang, W.; Lu, H.; Song, K.; Zhao, J. Stable high-power saturable absorber based on polymer-black-phosphorus films. *Opt. Commun.* **2018**, *406*, 254-259, doi:https://doi.org/10.1016/j.optcom.2016.11.027.

106. Sheik-Bahae, M.; Said, A.A.; Wei, T.; Hagan, D.J.; Stryland, E.W.V. Sensitive measurement of optical nonlinearities using a single beam. *IEEE J. Quantum Electron.* **1990**, *26*, 760-769, doi:10.1109/3.53394.

107. Woodward, R.; Howe, R.; Hu, G.; Torrisi, F.; Zhang, M.; Hasan, T.; Kelleher, E. Few-layer MoS 2 saturable absorbers for short-pulse laser technology: current status and future perspectives. *Photonics Res.* **2015**, *3*, A30-A42.

108. Jeon, J.; Lee, J.; Lee, J.H. Numerical study on the minimum modulation depth of a saturable absorber for stable fiber laser mode locking. *JOSA B* **2015**, *32*, 31-37.

109. Haiml, M.; Grange, R.; Keller, U. Optical characterization of semiconductor saturable absorbers. *Appl. Phys. B* **2004**, *79*, 331-339, doi:10.1007/s00340-004-1535-1.

110. Zhang, Y.; Lu, D.; Yu, H.; Zhang, H. Low-Dimensional Saturable Absorbers in the Visible Spectral Region. *Adv. Opt. Mater.* **2019**, *7*, 1800886, doi:https://doi.org/10.1002/adom.201800886.

111. Du, J.; Zhang, M.; Guo, Z.; Chen, J.; Zhu, X.; Hu, G.; Peng, P.; Zheng, Z.; Zhang, H. Phosphorene quantum dot saturable absorbers for ultrafast fiber lasers. *Sci. Rep.* **2017**, *7*, 42357, doi:10.1038/srep42357.

112. Guo, B. 2D noncarbon materials-based nonlinear optical devices for ultrafast photonics. *Chin. Opt. Lett.* **2018**, *16*, 020004.

113. Cui, Y.; Lu, F.; Liu, X. Nonlinear Saturable and Polarization-induced Absorption of Rhenium Disulfide. *Sci. Rep.* **2017**, *7*, 40080, doi:10.1038/srep40080.

114. Han, S.; Zhou, S.; Liu, X.; Liu, Y.; Zhang, S.; Yang, X. Rhenium disulfide-based passively Q-switched dual-wavelength laser at 0.95 μm and 1.06 μm in Nd:YAG. *Laser Phys. Lett.* **2018**, *15*, 085804, doi:10.1088/1612-202x/aac983.

115. Xu, X.; Jiang, M.; Li, D.; Wang, R.; Ren, Z.; Bai, J. Passive Q-switching based on ReS2 saturable absorber in Er-doped fiber laser at 1532 nm. *Opt Quantum Electron* **2018**, *50*, 39, doi:10.1007/s11082-017-1281-3.

116. Zhou, Y.; Fang, C.; Zhang, Z.; Tong, L.; Ma, X.; Zhang, W.; Yu, R.; Gao, W.; Xu, J.; Liao, M.; et al. Sub-picosecond passively mode-locked thulium-doped fiber laser by ReS2 nanoparticles. *Jpn. J. Appl. Phys.* **2020**, *60*, 011001, doi:10.35848/1347-4065/abd309.

117. Zuo, C.; Cao, Y.; Yang, Q.; He, J.; Zhang, B. Passively Q-switched 2.95-μm bulk laser based on rhenium disulfide as saturable absorber. *IEEE Photon. Technol. Lett.* **2019**, *31*, 206-209, doi:10.1109/LPT.2018.2886784.

118. Su, X.; Zhang, B.; Wang, Y.; He, G.; Li, G.; Lin, N.; Yang, K.; He, J.; Liu, S. Broadband rhenium disulfide optical modulator for solid-state lasers. *Photonics Res.* **2018**, *6*, 498-505, doi:10.1364/PRJ.6.000498.

119. Liu, S.; Wang, M.; Yin, S.; Xie, Z.; Wang, Z.; Zhou, S.; Chen, P. Nonlinear Optical Properties of Few-Layer Rhenium Disulfide Nanosheets and Their Passively Q-switched Laser Application. *Phys. Status Solidi A* **2019**, *216*, 1800837.

120. Lin, M.; Peng, Q.; Hou, W.; Fan, X.; Liu, J. 1.3 μm Q-switched solid-state laser based on few-layer ReS2 saturable absorber. *Opt. Laser Technol.* **2019**, *109*, 90-93, doi:https://doi.org/10.1016/j.optlastec.2018.07.062.

121. Zhang, S.; Ma, Y.; Liu, X.; Ding, S.; Yu, X.; Zhang, Q. Continuous wave and rhenium disulfide passively Q-switched Nd:GdLaNbO4 laser under direct pumping. *Opt. Commun.* **2020**, *473*, 125977, doi:https://doi.org/10.1016/j.optcom.2020.125977.

122. Zhang, N.; Zeng, Z.; Wang, Z.; Li, B.; Pan, Y. Nd:YSAG Q-switched laser with anisotropic ReS2 nanosheets. *Optik* **2020**, *208*, 164542, doi:https://doi.org/10.1016/j.ijleo.2020.164542.

123. Su, X.; Nie, H.; Wang, Y.; Li, G.; Yan, B.; Zhang, B.; Yang, K.; He, J. Few-layered ReS 2 as saturable absorber for 2.8 μm solid state laser. *Opt. Lett.* **2017**, *42*, 3502-3505.

124. Fan, M.; Li, T.; Zhao, J.; Zhao, S.; Li, G.; Yang, K.; Su, L.; Ma, H.; Kränkel, C. Continuous wave and ReS2 passively Q-switched Er : SrF2 laser at ~3 μm. *Opt. Lett.* **2018**, *43*, 1726-1729, doi:10.1364/OL.43.001726.

125. Lu, B.; Wen, Z.; Huang, K.; Qi, X.; Wang, N.; Chen, H.; Bai, J. Passively Q-Switched Yb3+-Doped Fiber Laser With ReS2 Saturable Absorber. *IEEE J. Sel. Top. Quantum Electron.* **2019**, *25*, 1-4, doi:10.1109/JSTQE.2018.2885493.

126. Mao, D.; Cui, X.; Gan, X.; Li, M.; Zhang, W.; Lu, H.; Zhao, J. Passively Q-Switched and Mode-Locked Fiber Laser Based on an ReS2 Saturable Absorber. *IEEE J. Sel. Top. Quantum Electron.* **2018**, *24*, 1-6, doi:10.1109/JSTQE.2017.2713641.

127. He, J.; Zeng, G.; Liu, S.; Lu, H.; Xie, R.; Qi, J.; Tao, L.; Zhou, B. Preparation of ultrathin ReS2 nanosheets and their application to Q-switched Er-doped fiber lasers. *Frontiers of Information Technology & Electronic Engineering* **2021**, *22*, 296-302, doi:10.1631/FITEE.2000339.

128. Zhao, R.; Li, G.; Zhang, B.; He, J. Multi-wavelength bright-dark pulse pair fiber laser based on rhenium disulfide. *Opt. Express* **2018**, *26*, 5819-5826.

129. Steinberg, D.; Zapata, J.D.; Souza, E.A.T.d.; Saito, L.A.M. Mechanically exfoliated Rhenium disulfide onto D-shaped optical fiber for sub-300 fs EDFL mode-locking. In Proceedings of the 2018 Conference on Lasers and Electro-Optics (CLEO), 13-18 May 2018, 2018; pp. 1-2.

130. Zhang, M.; Yin, J.; Yan, P. Two-dimensional ReS2 nanosheets based saturable absorbers for passively mode-locked fiber lasers. In Proceedings of the CLEO Pacific Rim Conference 2018, Hong Kong, 2018/07/29, 2018; p. W3A.151.

131. Cui, Q.; He, J.; Bellus, M.Z.; Mirzokarimov, M.; Hofmann, T.; Chiu, H.Y.; Antonik, M.; He, D.; Wang, Y.; Zhao, H. Transient absorption measurements on anisotropic monolayer ReS2. *Small* **2015**, *11*, 5565-5571.

132. Trushin, M.; Kelleher, E.J.R.; Hasan, T. Theory of edge-state optical absorption in two-dimensional transition metal dichalcogenide flakes. *Phys. Rev. B* **2016**, *94*, 155301, doi:10.1103/PhysRevB.94.155301.

133. Mao, D.; Zhang, S.; Wang, Y.; Gan, X.; Zhang, W.; Mei, T.; Wang, Y.; Wang, Y.; Zeng, H.; Zhao, J. WS 2 saturable absorber for dissipative soliton mode locking at 1.06 and 1.55 μm. *Opt. Express* **2015**, *23*, 27509-27519.

134. Wang, S.; Yu, H.; Zhang, H.; Wang, A.; Zhao, M.; Chen, Y.; Mei, L.; Wang, J. Broadband few-layer MoS2 saturable absorbers. *Adv. Mater.* **2014**, *26*, 3538-3544.

135. Woodward, R.I.; Kelleher, E.J.R.; Howe, R.C.T.; Hu, G.; Torrisi, F.; Hasan, T.; Popov, S.V.; Taylor, J.R. Tunable Q-switched fiber laser based on saturable edge-state absorption in few-layer molybdenum disulfide (MoS2). *Opt. Express* **2014**, *22*, 31113-31122, doi:10.1364/OE.22.031113.

136. Wang, K.; Feng, Y.; Chang, C.; Zhan, J.; Wang, C.; Zhao, Q.; Coleman, J.N.; Zhang, L.; Blau, W.J.; Wang, J. Broadband ultrafast nonlinear absorption and nonlinear refraction of layered molybdenum dichalcogenide semiconductors. *Nanoscale* **2014**, *6*, 10530-10535, doi:10.1039/C4NR02634A.

137. Horzum, S.; Çakır, D.; Suh, J.; Tongay, S.; Huang, Y.-S.; Ho, C.-H.; Wu, J.; Sahin, H.; Peeters, F. Formation and stability of point defects in monolayer rhenium disulfide. *Phys. Rev. B* **2014**, *89*, 155433.

138. Karatay, A.; Yaglioglu, H.G.; Elmali, A.; Parlak, M.; Karaagac, H. Thickness-dependent nonlinear absorption behaviors in polycrystalline ZnSe thin films. *Opt. Commun.* **2012**, *285*, 1471-1475, doi:https://doi.org/10.1016/j.optcom.2011.11.088.

139. Yu, Z.; Song, Y.; Tian, J.; Dou, Z.; Guoyu, H.; Li, K.; Li, H.; Zhang, X. High-repetition-rate Q-switched fiber laser with high quality topological insulator Bi2Se3 film. *Opt. Express* **2014**, *22*, 11508-11515, doi:10.1364/OE.22.011508.

140. Li, H.; Xia, H.; Lan, C.; Li, C.; Zhang, X.; Li, J.; Liu, Y. Passively Q-switched erbium-doped fiber laser based on few-layer MoS 2 saturable absorber. *IEEE Photon. Technol. Lett.* **2014**, *27*, 69-72.